Mon. Not. R. Astron. Soc. **000**, 1–27 (2011) Printed 7 January 2011 (MN LATEX style file v2.2)

The ATLAS^{3D} project – I. A volume-limited sample of 260 nearby early-type galaxies: science goals and selection criteria

Michele Cappellari[1⋆], Eric Emsellem[2,3], Davor Krajnović[2], Richard M. McDermid [4], Nicholas Scott[1], G. A. Verdoes Kleijn[5], Lisa M. Young[6], Katherine Alatalo[7], R. Bacon[3], Leo Blitz[7], Maxime Bois[2,3], Frédéric Bournaud[8], M. Bureau[1], Roger L. Davies[1], Timothy A. Davis[1], P. T. de Zeeuw[2,9], Pierre-Alain Duc[10], Sadegh Khochfar[11], Harald Kuntschner[12], Pierre-Yves Lablanche[3], Raffaella Morganti[5,13], Thorsten Naab[14], Tom Oosterloo[5,13], Marc Sarzi[15], Paolo Serra[13], and Anne-Marie Weijmans[16]†

[1]*Sub-department of Astrophysics, University of Oxford, Denys Wilkinson Building, Keble Road, Oxford OX1 3RH*
[2]*European Southern Observatory, Karl-Schwarzschild-Str. 2, 85748 Garching, Germany*
[3]*Université Lyon 1, Observatoire de Lyon, Centre de Recherche Astrophysique de Lyon and Ecole Normale Supérieure de Lyon, 9 avenue Charles André, F-69230 Saint-Genis Laval, France*
[4]*Gemini Observatory, Northern Operations Centre, 670 N. A'ohoku Place, Hilo, HI 96720, USA*
[5]*Kapteyn Astronomical Institute, University of Groningen, Postbus 800, 9700 AV Groningen, The Netherlands*
[6]*Physics Department, New Mexico Institute of Mining and Technology, Socorro, NM 87801, USA*
[7]*Department of Astronomy, Campbell Hall, University of California, Berkeley, CA 94720, USA*
[8]*Laboratoire AIM Paris-Saclay, CEA/IRFU/SAp CNRS Université Paris Diderot, 91191 Gif-sur-Yvette Cedex, France*
[9]*Sterrewacht Leiden, Leiden University, Postbus 9513, 2300 RA Leiden, the Netherlands*
[10]*Laboratoire AIM, CEA/DSM-CNRS-Universit Paris Diderot, Dapnia/Service d'Astrophysique, CEA-Saclay, 91191 Gif-sur-Yvette Cedex, France*
[11]*Max-Planck Institut für extraterrestrische Physik, PO Box 1312, D-85478 Garching, Germany*
[12]*Space Telescope European Coordinating Facility, European Southern Observatory, Karl-Schwarzschild-Str. 2, 85748 Garching, Germany*
[13]*Netherlands Institute for Radio Astronomy (ASTRON), Postbus 2, 7990 AA Dwingeloo, The Netherlands*
[14]*Max-Planck Institut für Astrophysik, Karl-Schwarzschild-Str. 1, 85741 Garching, Germany*
[15]*Centre for Astrophysics Research, University of Hertfordshire, Hatfield, Herts AL1 9AB, UK*
[16]*Dunlap Institute for Astronomy & Astrophysics, University of Toronto, 50 St. George Street, Toronto, ON M5S 3H4, Canada*

Accepted 2010 December 3. Received 2010 November 2

ABSTRACT

The ATLAS^{3D} project is a multi-wavelength survey combined with a theoretical modelling effort. The observations span from the radio to the millimeter and optical, and provide multi-colour imaging, two-dimensional kinematics of the atomic (H I), molecular (CO) and ionized gas (Hβ, [O III] and [N I]), together with the kinematics and population of the stars (Hβ, Fe5015 and Mg *b*), for a carefully selected, volume-limited (1.16×10^5 Mpc^3) sample of 260 early-type (elliptical E and lenticular S0) galaxies (ETGs). The models include semi-analytic, N-body binary mergers and cosmological simulations of galaxy formation. Here we present the science goals for the project and introduce the galaxy sample and the selection criteria. The sample consists of nearby ($D < 42$ Mpc) morphologically-selected ETGs extracted from a *parent* sample of 871 galaxies (8% E, 22% S0 and 70% spirals) brighter than $M_K < -21.5$ mag (stellar mass $M_\star \gtrsim 6 \times 10^9\ M_\odot$). We analyze possible selection biases and we conclude that the parent sample is essentially complete and statistically representative of the nearby galaxy population. We present the size-luminosity relation for the spirals and ETGs and show that the ETGs in the ATLAS^{3D} sample define a tight red sequence in a colour-magnitude diagram, with few objects in the transition from the blue cloud. We describe the strategy of the SAURON integral-field observations and the extraction of the stellar kinematics with the pPXF method. We find typical 1σ errors of $\Delta V \approx 6$ km s^{-1}, $\Delta\sigma \approx 7$ km s^{-1}, $\Delta h_3 \approx \Delta h_4 \approx 0.03$ in the mean velocity, the velocity dispersion and Gauss-Hermite (GH) moments for galaxies with effective dispersion $\sigma_e \gtrsim 120$ km s^{-1}. For galaxies with lower σ_e (≈ 40% of the sample) the GH moments are gradually penalized by pPXF towards zero to suppress the noise produced by the spectral under-sampling and only V and σ can be measured. We give an overview of the characteristics of the other main datasets already available for our sample and of the ongoing modeling projects.

Key words: galaxies: classification – galaxies: elliptical and lenticular, cD – galaxies: evolution – galaxies: formation – galaxies: structure – galaxies: kinematics and dynamics

1 INTRODUCTION

1.1 Scientific background

Observations of high-redshift galaxies and the cosmic microwave background (Spergel et al. 2007) have revealed the Universe to be dominated by dark matter and dark energy (Riess et al. 1998; Perlmutter et al. 1999), providing a working paradigm for the formation of structure (e.g. Springel et al. 2005). However, the mechanisms that form the luminous content of the dark-matter potential (i.e. the stars and galaxies that we observe) remain the key unknowns of modern extra-galactic astronomy. These processes are driven by the hydrodynamics and chemistry of the gas, combined with complex radiative feedback processes. High-redshift observations alone are not sufficient to constrain these processes, lacking spectral information and spatial resolution (Faber et al. 2007). It is therefore necessary to complement these studies with detailed analysis of nearby objects, tracing the *fossil record* of the formation process. Early-type (elliptical E and lenticular S0) galaxies (ETGs) are especially useful as they are old, have smaller levels of star formation and limited amount of dust, which simplifies the interpretation of the observations. Significant progress has been made in this direction in the past few decades, building on the classic observational works that still capture much of our understanding of the structure of local ETGs (e.g. Hubble 1936; Faber & Jackson 1976; Davies et al. 1983; Dressler et al. 1987; Djorgovski & Davis 1987; Bender et al. 1992; Kormendy & Richstone 1995).

A major step forward was brought by the era of large galaxy surveys. Thanks to the unprecedented sample size, one of the most important contributions of the Sloan Digital Sky Survey (SDSS, York et al. 2000) was to firmly establish a statistically significant bimodality in the colour distribution of local galaxies, such that they can be clearly separated in a so-called 'blue cloud', generally consisting of star-forming spiral galaxies, and a 'red sequence', mostly of non-star-forming ETGs (Strateva et al. 2001; Baldry et al. 2004). Accurately quantifying this bimodality, and the realization that it can be traced back in time to higher redshift (Bell et al. 2004; Faber et al. 2007), allowed a dramatic improvement in the detailed testing of galaxy formation scenarios.

The bimodality can only be explained with the existence of a mechanism, which suppresses episodes of intense star formation by evacuating gas from the system, resulting in a rapid transition of galaxies from the blue cloud to the red sequence (Springel et al. 2005; Faber et al. 2007). Many simulation groups have reproduced the bimodality qualitatively, though with rather different assumptions for the star formation and feedback processes (Granato et al. 2004; Di Matteo et al. 2005; Bower et al. 2006; Cattaneo et al. 2006; Croton et al. 2006). A generic feature of these models is that red-sequence galaxies form by dissipational 'wet mergers' of gas-rich blue-cloud galaxies, followed by quenching of the resulting intense star-formation by rapid ejection of the gas, caused by the feedback from a central supermassive black hole, supernovae winds, by shock heating of the gas in the most massive halos (Kereš et al. 2005; Dekel & Birnboim 2006) or gravitational gas heating (Naab et al. 2007; Khochfar & Ostriker 2008; Johansson et al. 2009). The merging of the most massive blue galaxies, however, is not sufficient to explain the population of most-massive red-sequence galaxies. Dissipationless 'dry mergers' of gas-poor, red-sequence galaxies is therefore also required, evolving galaxies *along* the red-sequence as they increase in mass (Khochfar & Burk-

⋆ E-mail: cappellari@astro.ox.ac.uk
† Dunlap Fellow

ert 2003; Naab et al. 2006; Hopkins et al. 2009; Khochfar & Silk 2009; Oser et al. 2010).

Both wet and dry major mergers generally produce red, bulge-dominated galaxies when feedback is included in the models. The kinematic structure of the remnants is however very different. In a major (1:1) merger between blue gas-rich galaxies, the gas tends to form a disk, so that the end result of the merger, after the gas has been removed from the system by ejection, heating or conversion to stars, will be a red stellar system dominated by rotation (Cox et al. 2006; Naab et al. 2006; Robertson et al. 2006; Jesseit et al. 2009). In major mergers between red gas-poor galaxies, dissipationless processes dominate, resulting in a red galaxy with little or no net rotation (Barnes 1992; Hernquist 1992; Naab et al. 1999; Naab & Burkert 2003; Cox et al. 2006). Unlike major mergers, minor mergers (1:3 or less) retain more closely the structure of the progenitor, to an extent that depends on the amount of mass and gas accreted, so that the remnant of a spiral galaxy will always display significant rotation (Naab et al. 2006; Robertson et al. 2006; Bournaud et al. 2007; Jesseit et al. 2009). These simulations demonstrate that if galaxies assemble by mergers, the existence of the red/blue galaxies dichotomy therefore also suggests the existence of a *kinematical* differentiation *within* the red sequence between fast and slow rotating galaxies.

Various classic observational indicators of an ETGs dichotomy have been proposed in the past two decades. ETGs have been found to exhibit trends as a function of luminosity in terms of (i) their distribution on the $(V/\sigma, \varepsilon)$ diagram, which relates the ratio of ordered V and random σ stellar motion to the galaxy ellipticity ε (e.g. Illingworth 1977; Binney 1978; Davies et al. 1983), (ii) their isophote shape (disky or boxy) (Bender et al. 1989; Kormendy & Bender 1996), (iii) the inner slope of their photometric profiles: cored/cuspy (Ferrarese et al. 1994; Lauer et al. 1995; Faber et al. 1997) or excess/deficit of core light (Graham 2004; Ferrarese et al. 2006; Kormendy et al. 2009). However, none of these signatures have been able to give clear evidence for a distinction between the two classes of red-sequence galaxies, primarily because they are all essentially secondary indicators of the galaxies' internal kinematic structure.

By the application of integral-field spectroscopy to a representative sample of nearby ETGs, the SAURON survey (de Zeeuw et al. 2002) has revealed the full richness of the kinematics of these objects (Emsellem et al. 2004; McDermid et al. 2006; Krajnović et al. 2008). From the two-dimensional nature of this unique data set, two distinct morphologies of stellar rotation fields are clearly evident, corresponding to the above described fast- and slow-rotators. In two companion papers of that survey a global quantitative measure of this morphology was defined, termed λ_R, that can be used to kinematically classify these galaxies in a way that is more robust than the $(V/\sigma, \varepsilon)$ diagram, is nearly insensitive to projection effects (Emsellem et al. 2007; Cappellari et al. 2007). λ_R relates directly to their formation, and is precisely reproducible in current cosmological simulations (Jesseit et al. 2009; Bois et al. 2010). This is the basic new finding we plan to exploit in the present project to improve our understanding of the structure and formation of ETGs. Additional results of the SAURON survey on ETGs include the robustness and empirical 'calibration' of the simple virial mass estimator to measure mass in the central parts of ETGs and a determination of their dark matter fraction (Cappellari et al. 2006). The survey found a high incidence of ionized gas in ETGs (Sarzi et al. 2006) and explained their ionization mechanism as mainly due to the evolved stellar population (Sarzi et al. 2010). It was shown that the stellar population gradients correlate well with the escape velocity, both locally within galaxies and globally among different ETGs (Scott et al. 2009). Star formation in ETGs only happens in fast rotators and follows two distinct modes: in disks or widespread (Shapiro et al. 2010), where the latter cases are in low-mass systems (Jeong et al. 2009; Kuntschner et al. 2010). Disks in fast rotators have enhanced metallicity, while kinematically distinct cores in slow rotators show no stellar population signatures (Kuntschner et al. 2006, 2010).

1.2 Goals of the Project

Due to the exploratory character of the SAURON survey (de Zeeuw et al. 2002), the ETGs were selected to sample, with a relatively small number of objects, a wide range of masses, shapes and morphologies. This was done by selecting galaxies brighter than a total magnitude $M_B < -18$ mag equally subdivided into 24 E and 24 S0. Within each E/S0 subclass the selected objects sample uniformly a grid in the (M_B, ε) plane. Although that approach was crucial in bringing the fast/slow rotator dichotomy to light and in most of the findings mentioned in the previous section, the selection criteria impose complex biases and do not allow for a quantitative statistical comparisons of galaxy properties with simulations, which is a main goal of the ATLAS^{3D} project. Moreover, with only 48 galaxies, the statistical uncertainties are large.

The power of the kinematic classification based on λ_R is to be able to study differences in the formation process along the red-sequence galaxy population. The λ_R parameter describes in a compact way the present status of the galaxies, however it is essential to obtain information on the formation history and the detailed dynamical structure as well. The stellar population contains a record of the more distant history (a few Gyr). Recent gas accretion is recorded in the cold atomic gas components, generally detected on galaxy scales with radio observations of H I, while the ongoing accretion and star formation activity is traced by cold molecular gas (e.g. CO), often detected in regular disks in the central regions. For comparison with theoretical predictions one needs to observe all these quantities for a statistically significant, volume-limited sample of galaxies complete to some useful lower limit in mass. With these ideas in mind we carefully selected the ATLAS^{3D} sample of ETGs and we systematically observed all the above quantities. The ATLAS^{3D} dataset now provides a complete inventory of the baryon budget and a detailed two-dimensional description of stellar and gaseous kinematics, together with resolved stellar population within the main body of a complete and statistically significant sample of ETGs. Our goal is to use this dataset to perform archeological cosmology by specifically answering the following questions:

(i) How do slow rotators form? What are the physical processes that determine their kinematic and photometric features? What is the role of major and minor mergers in their formation history? This will be reflected in the kinematics, gas content and stellar population.

(ii) Why are most ETGs fast rotators? There seems to be a dominant formation mechanism that delivers galaxies with quite homogenous rotation properties. Can this be merging? Can significant major merging be excluded?

(iii) How is star formation in ETGs quenched? Is it different for fast and slow rotators ETGs? How does it depend on environment? Can we infer the quenching mechanism from the amount and distribution of the left-over gas, the presence of AGNs or metallicity

gradients? The distribution of stellar population and gas properties constitute a stringent test for future galaxy formation models.

(iv) Most past studies have focused on single stellar population models of ETGs, but cosmological models predict more complex histories. Can we infer the star formation history in ETGs for detailed comparison with simulations?

(v) How do counter rotating cores in massive and old ETGs form and survive to the present time? Are these relics of the very early Universe?

(vi) Can we link the present day properties of ETGs to results form existing and upcoming surveys at higher redshift with respect to e.g. masses, sizes, stellar populations, gas fractions, star formation? Our study will constitute a $z = 0$ redshift benchmark to trace the time evolution of galaxies.

The ATLAS^{3D} sample includes all nearby ETGs observable from the northern Earth hemisphere, and for this reason we hope its homogeneous dataset will ultimately constitute a legacy for future studies. We trust that our and other groups will exploit our data and sample well beyond what we had originally envisioned. Our first steps in the directions outlined above are presented in the following papers, while the other aspects will be presented in subsequent papers of this series:

(i) Krajnović et al. (2011, hereafter Paper II), which describes the morphology of the kinematics and the kinematical misalignment in ETGs;

(ii) Emsellem et al. (2011, hereafter Paper III), which presents a census of the stellar angular momentum in the central region of ETGs;

(iii) Young et al. (2011, hereafter Paper IV), which quantifies the distribution of molecular gas content in ETGs;

(iv) Davis et al. (2011, hereafter Paper V), which studies the Tully & Fisher (1977) relation from the width of the molecular lines in ETGs;

(v) Bois et al. (2011, hereafter Paper VI), which studies the formation of the fast and slow-rotator galaxies via numerical simulations of binary mergers;

(vi) Cappellari et al. (2011, hereafter Paper VII), which revisits the morphology of nearby galaxies and presents the *kinematic* morphology-density relation.

Here in Section 2 we discuss the selection criteria for the *parent* sample of galaxies, from which the ATLAS^{3D} sample of ETGs was extracted (Section 3). In Section 4 we present the SAURON observing strategy for the survey, the integral-field data, and the kinematic extraction, while other additional datasets and simulations from our project are listed in Section 5. We give a summary in Section 6. In the paper we assume $H_0 = 72$ km s^{-1} Mpc^{-1}.

2 THE PARENT SAMPLE

2.1 Selection criteria

Our final ATLAS^{3D} sample will focus on ETGs only, however before any morphological classification, we want to select all galaxies in the nearby volume above a certain total stellar mass. As we did not have dynamical information for all galaxies in the local volume at the beginning of our survey, the best proxy for mass available was the near-infrared (~ 2.2 μm) K_s-band luminosity provided by the two-micron all sky redshift survey (2MASS; Skrutskie & et al. 2006), which is unique for its full sky completeness and excellent photometric homogeneity. The K_s-band is 5–10 times less sensitive to dust absorption than optical wavelengths and therefore can be used to select both dust-rich spirals and dust-poor ETGs to a similar mass level. Moreover the mass-to-light ratio of the stars in the near infrared varies only about a factor ≈ 2, which is $\sim 3\times$ less than at optical wavelengths (Bell et al. 2001; Maraston 2005), thus providing a better approximation to the stellar mass than an optical selection.

To derive luminosities from the observed apparent magnitudes we need distances. Numerous accurate determinations have been accumulated in the literature in the past few years. But we will resort to redshift distances when a more accurate distance is not available. In addition we enforce obvious observability criteria. This leads to the following selection steps:

(i) Choose a representative local volume with radius $D = 42$ Mpc. It approximates the redshift selection $cz < 3000$ km s^{-1} of the SAURON survey, for an adopted $H_0 = 72$ km s^{-1} Mpc^{-1} (Dunkley et al. 2009). It makes sure that key spectral features, such as Hβ, [O III] and Mg *b*, fall within the SAURON wavelength range and allows for a significant overlap with previous observations;

(ii) Specify the observability criterion from the William Herschel Telescope on La Palma $|\delta - 29^\circ| < 35^\circ$, where δ is the sky declination;

(iii) Exclude the dusty region near the Galaxy equatorial plane $|b| < 15^\circ$, with b the galactic latitude;

(iv) Select all galaxies from the 2MASS extended source catalog (XSC; Jarrett et al. 2000) with apparent total magnitude $K_T < 11.6$ mag (defined by the XSC parameter k_m_ext) and satisfying the observability criteria (ii)-(iii). Given the near completeness of the XSC down to $K_T \approx 13.5$, this selection is essentially complete. It ensures that all candidate galaxies brighter than an absolute total magnitude $M_K = K_T - 5\log D - 25 = -21.5$ mag are selected. This K_s-band luminosity limit roughly corresponds to a B-band selection $M_B \lesssim -18$, for the typical $B - K_s \approx 3.5$ mag colour of ETGs, at the faint end of our selection. This criterion is thus again similar to the one in the SAURON survey and allows for a significant overlap in the samples, reducing the required observing time. This step provides a sample of $\sim 20,000$ extended objects classified as galaxies;

(v) Assign a distance to as many galaxies as possible in the selection and include in the ATLAS^{3D} parent sample the ones with $D < 42$ Mpc and $M_K < -21.5$ mag; The distance selection requires some further explanation and may introduce incompleteness biases which are discussed in the next section.

A summary of the selection criteria is given in Table 1, while some of the main characteristics of the resulting galaxy sample are given in Table 2. This is the sample of galaxies, which includes both spiral and ETGs, from which the ATLAS^{3D} sample of ETGs will be extracted. The names and the characteristics of the resulting 871 galaxies in the ATLAS^{3D} parent sample are given in Table 5 (for the ETGs) and Table 6 (for the spirals). As the evolution of spirals and ETGs are closely related, the spirals of the parent sample are critical to properly interpret the ATLAS^{3D} results on ETGs.

2.2 Sources of distances and errors

Numerous sources of distances for nearby galaxies have been accumulated over the past decades. In most cases the distances are based on redshift as provided by large redshift surveys, but a number of more accurate distances are available based on other methods (see

Table 1. Selection criteria for the galaxies in the ATLAS^{3D} parent sample

Distance:	$D < 42$ Mpc
Galaxies total mag:	$M_K < -21.5$ mag
Observability:	$\|\delta - 29°\| < 35°$
Galaxy zone of avoidance:	$\|b\| > 15°$

Table 2. Main characteristics of the ATLAS^{3D} parent sample

Survey Volume:	Vol $= 1.16 \times 10^5$ Mpc^3
Galaxy K-band luminosity:	$L > 8.2 \times 10^9\ L_{K,\odot}$
Galaxy stellar mass:	$M_\star \gtrsim 6 \times 10^9\ M_\odot$
Galaxy B-band total mag:	$M_B \lesssim -18.0$ mag
Galaxy SDSS r-band total mag:	$M_r \lesssim -18.9$ mag
Total number of galaxies:	$N_{\rm gal} = 871$
Spiral and irregular galaxies:	$N_{\rm Sp} = 611$ (70%)
S0 galaxies in ATLAS^{3D} ($T > -3.5$):	$N_{\rm S0} = 192$ (22%)
E galaxies in ATLAS^{3D} ($T \leq -3.5$):	$N_{\rm E} = 68$ (8%)

e.g. the recent compilations of Tully et al. 2008, 2009; Karachentsev & Nasonova 2010). For the $\sim 20,000$ 2MASS galaxies with $M_K < -21.5$ mag we tried to automatically assign the most accurate available distance according to the following order of priority:

(i) Distance obtained with the surface brightness fluctuation (SBF) method for the ACS Virgo Cluster Survey (Mei et al. 2007; Blakeslee et al. 2009) (91 values). These are claimed to be accurate to about 3% in distance;

(ii) SBF distance from ground-based observation from Tonry et al. (2001) (300 values), which have a median error of 10% in distance. These have been converted to the same zeropoint of Mei et al. (2007) by subtracting 0.06 mag to the distance moduli (see discussion in Blakeslee et al. 2010);

(iii) Distances from the NED-D compilation[1] by Madore, Steer and the NED team (V3.0 June 2010, about 2000 values). The list includes accurate determinations using (1) SBF, (2) the tip of the red giant branch (TRGB), (3) Cepheids variables, with a claimed comparable accuracy of $\sim 10\%$, but the list also includes various other methods like the ones based on the (4) Tully & Fisher (1977) or (5) Fundamental Plane (Djorgovski & Davis 1987; Dressler et al. 1987) relations, on the (6) luminosity of Type Ia Supernovae, or on the luminosity functions of (7) globular clusters and (8) planetary nebulae. The latter methods are expected to be accurate to better than $\lesssim 20\%$ (Tully et al. 2008). For a number of galaxies more than one independent distance was available and we adopted the median of the values.

(iv) When no better distance was available, for galaxies within 12° of the projected center of the Virgo cluster (defined by the galaxy M87) with heliocentric radial velocities $V_{\rm hel} < 2300$ km s^{-1}, we assigned the distance of the cluster (assumed to be 16.5 Mpc from Mei et al. 2007). These distances should be accurate to $\sim 7\%$, considering the intrinsic depth of the cluster. Two galaxies were later removed from Virgo as that distance implied a too high and non-physical dynamical M/L as determined in Cappellari et al. 2010.

(v) Finally if none of the above criteria was met, we assigned a distance based on the observed heliocentric radial velocities $V_{\rm hel}$, which we converted to velocities $V_{\rm cosmic}$ characteristic of the expansion of the universe following Mould et al. (2000),[2] but only including the contribution of the Virgo attractor, and assuming $H_0 = 72$ km s^{-1} Mpc^{-1} (Dunkley et al. 2009). We repeated our sample selection using heliocentric velocities extracted from either the HyperLeda[3] (Paturel et al. 2003) or NED [4] databases and obtained identical final ATLAS^{3D} samples. We compared the $V_{\rm hel}$ of galaxies from NED and HyperLeda and found a general very good agreement in the two databases, with a biweight rms scatter of

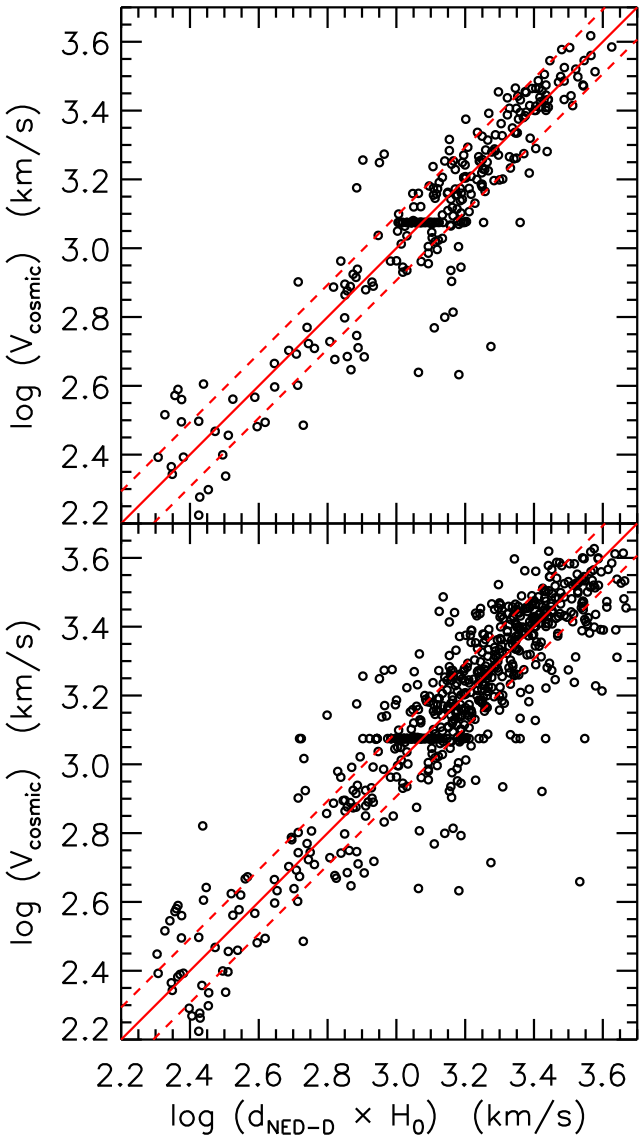

Figure 1. Accuracy of redshift distances. *Top Panel:* Recession velocities, converted into velocities $V_{\rm cosmic}$ characteristic of the expansion of the universe, against the median of the NED-D redshift-independent distances for 291 galaxies with at least 3 independent determination (in most cases including SBF distances). The solid line is a one-to-one relation, while the dashed lines indicate $\pm 24\%$ deviations. *Bottom Panel:* Same as in the top panel for 705 galaxies with at least one distance determination in NED-D.

[1] http://nedwww.ipac.caltech.edu/Library/Distances/

[2] Corrected as described in the corresponding Erratum.

[3] http://leda.univ-lyon1.fr/

[4] http://nedwww.ipac.caltech.edu/

0.4%, as expected given that in most cases the redshifts come from the same source. However in some cases significant differences exists: we found $83/5398$ galaxies (1.5%) with $V_{\rm hel}$ differences larger than 20%. For our $V_{\rm hel}$ in the parent sample we adopted NED (June 2010), which currently includes as major sources the Center for Astrophysics Redshift Catalog (Huchra et al. 1983), the RC3 (de Vaucouleurs et al. 1991), the ZCAT compilation (Huchra et al. 1992) and the Sloan Digital Sky Survey DR7 (Abazajian et al. 2009). After obtaining our new accurate SAURON redshifts (Section 4.3) we updated the redshift-based distances and this lead to the removal of one observed galaxy. However we retained in the sample two observed galaxies formally with $D > 42$ Mpc, but still inside our volume within the distance errors.

To estimate the representative errors of the redshift distances we correlated them against the direct distance estimates in the NED-D compilation. Specifically we selected the 285 galaxies in common with our sample with at least 3 independent distance determinations (in most cases including SBF distances), and we correlated the median of their $d_{\rm NED-D} \times H_0$ values against the $V_{\rm cosmic}$ (Fig. 1). We found a biweight dispersion of 24% in the residuals. The minimum value in the median residual was obtained with $H_0 = 72$ km s^{-1} Mpc^{-1}, consistent with the adopted WMAP estimate. Assuming a typical rms error of 10% for the best set of NED-D distances, this implies an intrinsic rms error of $\sim 21\%$ in the redshift distances. However a significant number of outliers exist. If we repeat the comparison for all the 692 galaxies in common, with a NED-D distance, the biweight dispersion increases to 29%, which would imply a redshift error of $\sim 27\%$. If we only consider the Local Group's peculiar velocity into Virgo in the calculation of $V_{\rm cosmic}$, the scatter increases significantly and systematic deviations appear. Including the infall of galaxies into the Virgo attractor improves the agreement. However including other attractors as done by Mould et al. (2000) does not appear to further reduce the scatter. For this reason we only included the more secure Virgo attractor contribution in our redshift distances corrections.

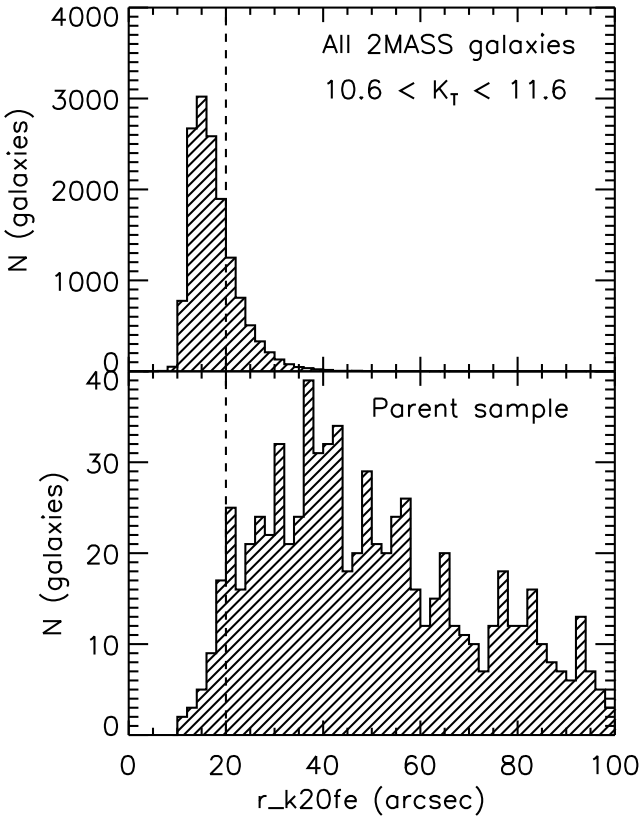

Figure 2. Apparent size distribution of 2MASS galaxies. *Top Panel:* The apparent size, as described by the 2MASS XSC parameter `r_k20fe`, for all the galaxies satisfying our observability criteria and with $10.6 < K_T < 11.6$. *Bottom Panel:* Same as in the top panel for the galaxies in the parent sample ($D < 42$ Mpc and $M_K < -21.5$ mag).

2.3 Estimating redshift incompleteness

Not all the $\sim 20,000$ 2MASS galaxies satisfying our observability criteria and with $K_T < 11.6$ have a redshift measurement. This may introduce biases in our volume limited sample selection. Specifically $4146/14461$ (29%) of the galaxies in the faintest magnitude bin $10.6 < K_T < 11.6$ do not have a redshift in NED.[5] The redshift completeness quickly improves for brighter apparent magnitudes, and in fact only 4% of the galaxies with $K_T < 10.6$ have no redshift. One way to estimate how many of these galaxies are likely to be within our selection criteria, is to look at their size distribution as measured by 2MASS. In fact one expects many of the apparently faint and small galaxies to be intrinsically brighter and larger, but to appear faint and small due to the large distance.

To quantify the galaxy angular sizes we use the 2MASS XSC parameter `r_k20fe`, which gives the semi-major axis of the 20 mag arcsec^{-2} surface brightness isophote at K_s. The size distribution for the galaxies in the faintest magnitude bin, according to this size parameter is shown in the top panel of Fig. 2. As expected the distribution presents a dramatic increase in the numbers for very small objects. For comparison we show in the bottom panel the size distribution of the 2MASS galaxies which satisfy our selection criteria $D < 42$ Mpc and $M_K < -21.5$ mag. The latter sample has a peak in the size distribution around `r_k20fe` $\approx 40''$, while the number of objects sharply drops for `r_k20fe` $\lesssim 20''$ (only 4% of the objects have sizes below that limit). This lack of apparently small objects is not due to any redshift selection criteria. In fact among all the galaxies with measured redshift, about equal numbers have size larger or smaller than `r_k20fe` $= 20''$. The apparent galaxy size is just an efficient way to select, without redshift information, galaxies unlikely to belong to our volume-limited sample.

Excluding all objects apparently smaller than `r_k20fe` $< 20''$, likely outside the limits of our local volume, we find a redshift incompleteness of $478/3383$ (14%) in the faintest magnitude bin. Among the galaxies that *do* have redshift in this set, only $68/2905$ (2%) satisfy the selection criteria for the parent sample (most of the others are still outside the local volume). This implies that statistically we may expect ~ 11 galaxies (1% of the parent sample) to be possibly missed from the parent sample due to redshift incompleteness in the faintest magnitude bin. We conclude that we can safely ignore this possible bias from any conclusion derived from the sample.

[5] The situation will change in the near future when the 2MASS Redshift Survey will become available, which is already complete down to $K_s = 11.25$ (Crook, et al. 2007) and ultimately aims for a redshift completeness down to $K_s = 13.0$ (Huchra et al. 2005).

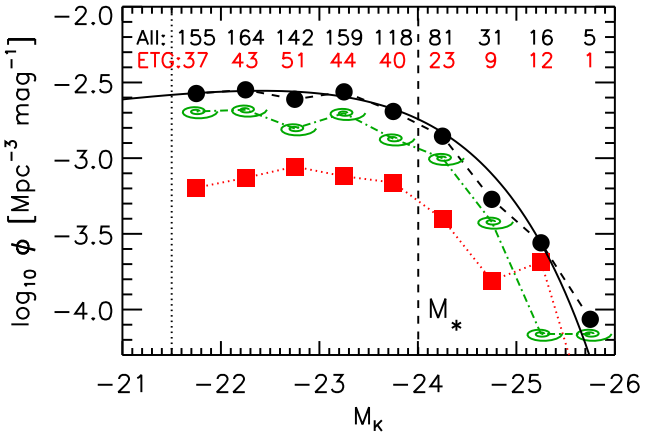

Figure 3. K_s-band luminosity function (LF) of the ATLAS^{3D} *parent* sample of 871 galaxies (black filled circles). The LF for the spiral galaxies (green spirals) and the 260 ETGs which constitute the ATLAS^{3D} sample (red squares) separately are also shown. The solid curve shows the Schechter (1976) function derived by Bell et al. (2003) from a fit to 6,282 galaxies. It was not fitted to our data! The black numbers above the symbols indicate the total number of galaxies included in each 0.5 mag bin, while the red ones are the corresponding numbers for the ETGs of the ATLAS^{3D} sample. There is no evidence of incompleteness down to the magnitude limit of the survey (vertical dotted line), which is ≈ 2.5 mag below $M_\star$ (vertical dashed line).

2.4 Luminosity function

The ATLAS^{3D} parent sample was carefully selected to provide a volume-limited sample of galaxies in the nearby universe. It should be representative of the galaxy population at low redshift, apart from the unavoidable cosmic variance, due to the relatively limited size of the volume. A first test of the representativeness of our parent sample is to compare its K_s-band luminosity function against that measured from larger volumes. For this we compare in Fig. 3 the luminosity function of the parent sample against that derived from a much larger sample, at a mean redshift $\langle z \rangle \approx 0.08$, by Bell et al. (2003), using 2MASS K_s-band photometry as we do, and SDSS redshifts. It agrees well with the ones by Kochanek et al. (2001) and Cole et al. (2001). The comparison shows excellent agreement between the two luminosity functions, both in shape and normalization, and indicates that our parent sample is representative of the general galaxy population. In particular this test shows no sign of incompleteness at the faint end, in agreement with the discussion of Section 2.3.

2.5 Size - Luminosity relations for spirals and ETGs

To illustrate the general characteristic of the galaxies in the parent sample Fig. 4 shows the K-band size-luminosity relation and the effective surface brightness $\Sigma_{50} \equiv L_{\odot K}/(2\pi {R_e}^2)$ for different morphological types. This plot shows a similar distribution as the one inferred from much larger galaxy samples based on SDSS photometry, further confirming the representativeness of our sample (compare Fig. 4 with fig. 2 of van Dokkum et al. 2008). In our plot we show the fast/slow rotator classification for 260 ETGs of the ATLAS^{3D} sample (Paper III) together with the early spirals (Sa–Sb) and later spiral types (Sc–Irr) of the parent sample. There is a clear trend in the $R_e - L_K$ diagram as a function of galaxy morphology. To quantify this trend we fitted linear relations to the logarithmic coordinates assuming the same fractional errors for both

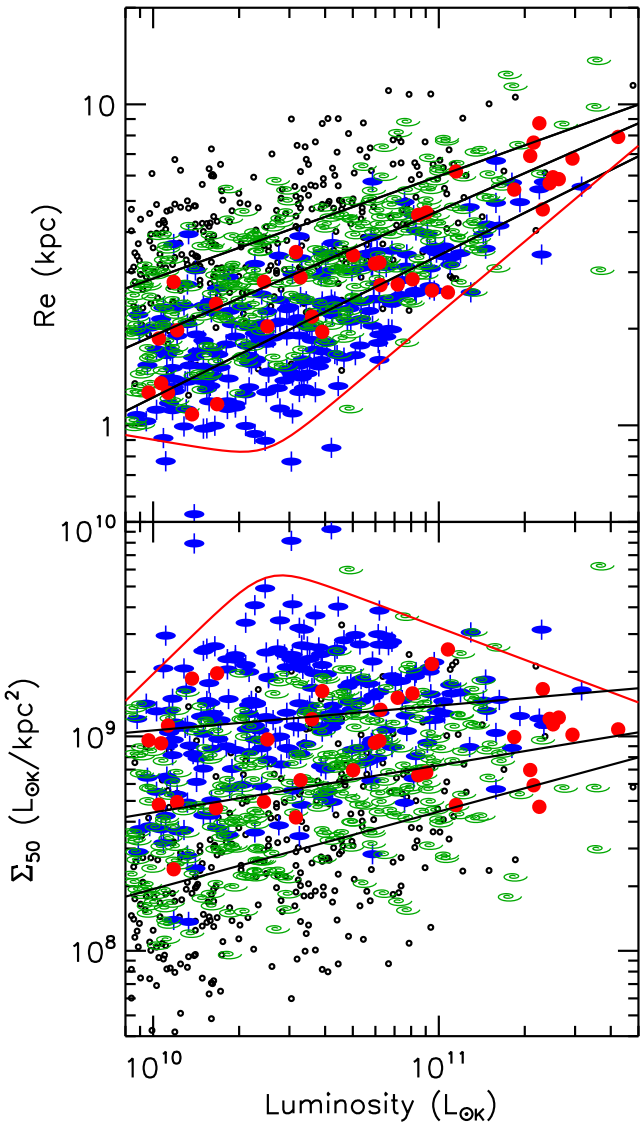

Figure 4. *Top Panel:* Size-Luminosity relation for the parent sample. The K-band luminosity of all the galaxies in the parent sample is plotted against the effective radius R_e (Section 4.1). Red filled circles are slow rotators, blue ellipses with vertical axis are fast rotators. These 260 objects constitute the ATLAS^{3D} sample. The green spirals represent spiral galaxies of type Sa–Sb ($-0.5 < T \leq 4$), while later spiral types ($T > 4$) are plotted as small open circles. The solid lines are the best fitting relations described in the text. From the bottom to the top they are fit to the fast rotators ETGs, to the Sa–Sb and to the later spiral types. The red curve approximates the boundary of the zone of avoidance in the observed galaxy distribution. *Bottom Panel:* Effective surface brightness versus luminosity. The symbols and the lines are the same as in the top panel.

axes and requiring $\chi^2/\mathrm{DOF} = 1$. The fit was performed using the `FITEXY` routine which is based on the algorithm by Press et al. (1992) and is part of the IDL Astronomy User's Library[6] (Landsman 1993). The best fitting power-law $R_e - L_K$ relations are

$$\log\left[\frac{R_e(\mathrm{FR})}{\mathrm{kpc}}\right] = 0.53 + 0.44\log\left[\frac{L_K(\mathrm{FR})}{10^{11}L_{\odot,K}}\right], \quad (1)$$

[6] Available from http://idlastro.gsfc.nasa.gov/

$$\log\left[\frac{R_{\rm e}({\rm Sa-Sb})}{\rm kpc}\right] = 0.67 + 0.39\log\left[\frac{L_K({\rm Sa-Sb})}{10^{11}L_{\odot,K}}\right], \quad (2)$$

$$\log\left[\frac{R_{\rm e}({\rm Sc-Irr})}{\rm kpc}\right] = 0.78 + 0.32\log\left[\frac{L_K({\rm Sc-Irr})}{10^{11}L_{\odot,K}}\right], \quad (3)$$

for fast rotators, Sa–Sb spirals and Sc or later spiral types respectively. There is a clear know zone of avoidance at small sizes and large luminosities, which is also well defined in our parent sample and approximated within the region where we have data by a double power-law (cfr. Lauer et al. 1995):

$$R_{\rm e} = 2^{(\gamma-\beta)/\alpha} R_{{\rm e},b}\left(\frac{L_K}{L_{K,b}}\right)^{\gamma}\left[1+\left(\frac{L_K}{L_{K,b}}\right)^{\alpha}\right]^{(\beta-\gamma)/\alpha}. \quad (4)$$

This equation defines a minimum effective radius $R_{{\rm e},b} = 0.85$ kpc and a corresponding maximum effective surface brightness at a characteristic galaxy luminosity $L_{K,b} = 2.5\times10^{10}$ L$_{\odot,K}$. The logarithmic power slope for $L_K \ll L_{K,b}$ is $\gamma = -0.15$, while for $L_K \gg L_{K,b}$ it is $\beta = 0.75$, so that for large luminosities $R_{\rm e} \propto L_K^{0.75}$. A sharp transition between the two regimes is set by $\alpha = 8$.

Consistently with other larger local galaxy samples (van Dokkum et al. 2008; Trujillo et al. 2009; Taylor et al. 2010), we find no massive and superdense ($L_K \gtrsim 10^{11}\ L_{\odot,K}$ and $R_{\rm e} \lesssim 2$ kpc) ETGs in our parent sample, contrary to what is found from photometry of ETGs at redshift $z \gtrsim 1.5$ (e.g. Daddi et al. 2005; Trujillo et al. 2006; Cimatti et al. 2008; van Dokkum et al. 2008). Similar $R_{\rm e}-L$ relations were derived by Shen et al. (2003) for early-type and late-type galaxies, defined as those having a Sersic (1968) index larger or smaller than $n = 2.5$ respectively. Their relation also showed a trend for late-types to have larger sizes (by definition, due to the smaller n) at given luminosity (or mass) and a more shallow $R_{\rm e}-L$ relations, as we find using the morphological selection. A trend in the $R_{\rm e}-M$ relation involving colours, with red-sequence galaxies having smaller sizes, can be seen in van Dokkum et al. (2008). While a trend involving age was presented by van der Wel et al. (2009) and Shankar & Bernardi (2009), and confirmed by Valentinuzzi et al. (2010), who find smaller sizes for older objects, at given stellar mass. All these trends are consistent with our finding using fast/slow rotators ETGs, in combination with traditional morphology of spiral galaxies (see also Bernardi et al. 2010), when one considers that later galaxy types tend to be more gas rich and have a younger stellar population. However here we interpret the observed trends as due to a variation in the bulge fraction, with bulges progressively increasing (by definition) from Sd-Sc to Sb-Sa and to fast rotators ETGs (see Paper VII). A detailed study of scaling relations in our sample will be presented in a subsequent paper.

3 THE ATLAS$^{\rm 3D}$ SAMPLE

3.1 Morphological selection

We established that the ATLAS$^{\rm 3D}$ parent sample is essentially complete within the selection criteria and representative of the nearby galaxy population. We also verified that its luminosity function agrees with the one derived from much larger volumes of the Universe. The ATLAS$^{\rm 3D}$ survey however is focused on the study of the fossil record of galaxy formation as recorded in the structure of ETGs. The ATLAS$^{\rm 3D}$ sample is a subset of the parent sample, consisting of all the ETGs in that sample.

The distinction between red-sequence and blue-cloud galaxies is related, but different from the early-type versus spiral morphological separation. E and S0 galaxies invariably lie on the red sequence, while late type spirals are generally on the blue cloud. However large fractions of spirals populate the red sequence as well and overlap with early-type galaxies (Strateva et al. 2001; Conselice 2006; van den Bergh 2007; Bernardi et al. 2010). An accurate morphology is easier to obtain for nearby galaxies and it is more robust than colour to dust and inclination effects. For this reasons a morphological classification is our preferred selection criterion.

To perform the morphological selection we considered using the morphological classification provided in available catalogues like the RC3 or its ongoing evolution HyperLeda. A problem with those classifications is the possible non-homogeneity of the classification process. Moreover the classification in those catalogues was performed using photometry in a single band, often from photographic plates. Given that for the majority of the galaxies in our parent sample excellent quality multi-band photometry is available from the SDSS DR7 (Abazajian et al. 2009), we decided to revisit the classification of the whole parent sample using the best available imaging.

The morphological classification of a given galaxy using multi-colour imaging may differ from the one obtained from photographic plates of the same object. Nonetheless we tried as much as possible to be consistent with the currently accepted morphological criteria. We just need to separate the parent sample into two classes: ETGs and spirals. This makes our task much simpler and reproducible than a more detailed morphological classification into E, S0 and spiral subclasses Sa–Sd.

Since the introduction of the classic tuning-fork diagram by Hubble (1936), for the past half century, essentially all authors have converged on a simple criterion to differentiate ETGs from spirals. The criterion, which defines the *revised* Hubble classification scheme, is outlined by Sandage (1961) in the Hubble Atlas and is based entirely on the presence of spiral arms (or dust lanes when seen edge-on): "The transition stages, S0 and SB0, are firmly established. In both sequences, the nebulae may be described as systems definitely later than E7 but showing no spiral structure". This same criterion was adopted unchanged in the extension to the classification scheme by de Vaucouleurs (1959, 1963), which was applied to the widely used RC2 and RC3 catalogues (de Vaucouleurs et al. 1976, 1991) and HyperLeda (Paturel et al. 2003). Although other characteristics of galaxies change with morphological classification (e.g. the bulge/disk ratio), they are ignored in the separation between early-types and spiral galaxies (see review by Sandage 1975). We adopted the same criterion here to select the ETGs belonging to the ATLAS$^{\rm 3D}$ sample from the parent sample.

Our morphological selection was done by visual inspection of the true-colour red-green-blue images (Lupton et al. 2004) provided by the SDSS DR7 which are available for 82% of the galaxies in the parent sample. For the remaining objects we used the B-band DSS2-blue images in the Online Digitized Sky Surveys[7]. We revisited the classification for the galaxies without SDSS DR7 data after obtaining our own INT imaging (Section 5.1) and this lead to the removal of a couple of galaxies from the ETGs sample. At the end of our classification we compared the agreement between our separation into early-types and spirals and the one provided by the T-type given by HyperLeda, which defines as ETGs (E and S0) those having $T \leq -0.5$. We found agreement in 97%

[7] http://archive.eso.org/dss

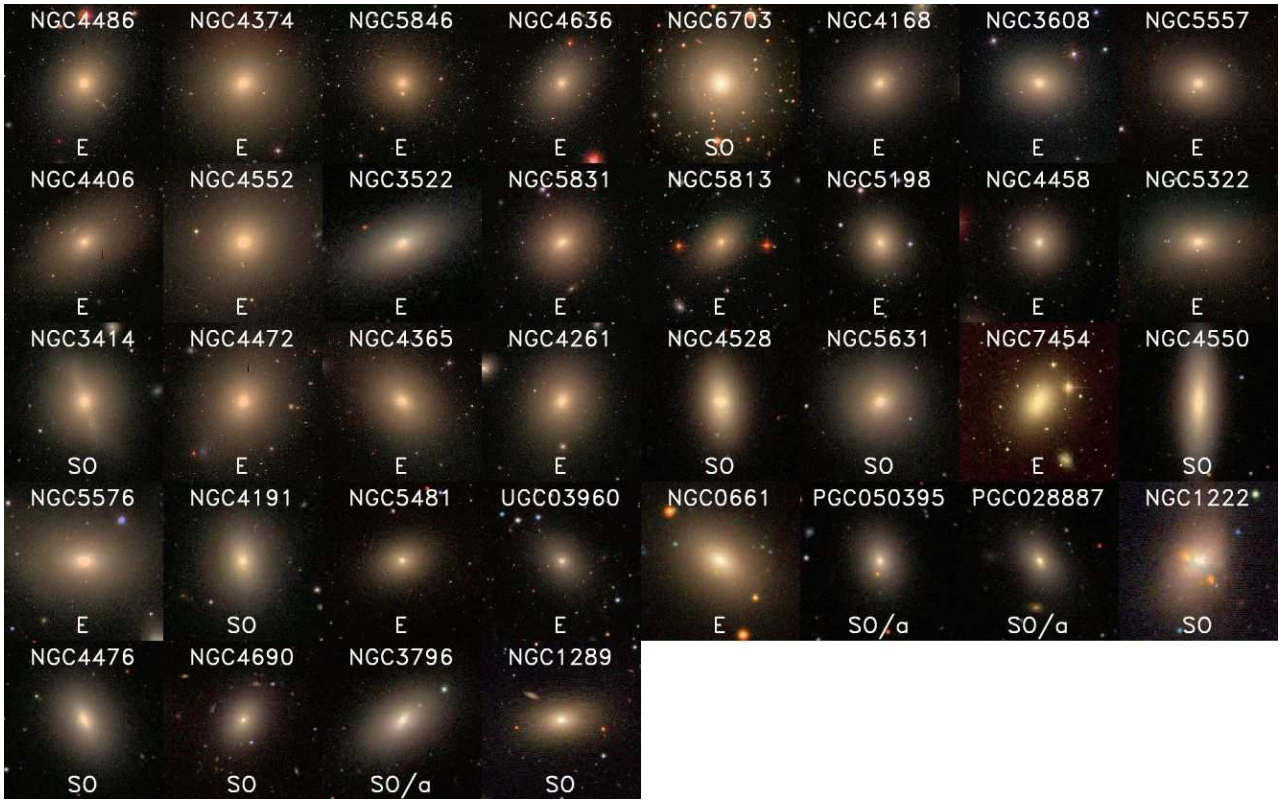

Figure 5. Morphology of slow rotators ETGs sorted by increasing λ_R. Postage stamps of the SDSS DR7 and INT red-green-blue composite images of slow rotators in the ATLAS^{3D} sample. The image of each galaxy was scaled so that the plot side is equal to $10R_e$, where R_e is the projected half-light radius given in Table 5. From left to right and from top to bottom the panels are sorted according to their specific stellar angular momentum, as measured by the parameter λ_R given in Paper III. The galaxy name is given at the top of each panel and the morphological classification from HyperLeda at the bottom. At this scale slow-rotator ETGs appear generally featureless except for the synchrotron jet in NGC 4486 and obvious signs of interactions in NGC 1222, NGC 3414 and NGC 5557. The only significant flat galaxy in this class is NGC 4550, while two other galaxies NGC 3796 and NGC 4528 show evidence of bar perturbations, which is typically associated to stellar disks. All these three objects contain counter-rotating stellar disks (Paper II). (This figure is better appreciated on a computer screen rather than on printed paper.)

of the cases, confirming the robustness and reproducibility of the morphological selection. The few disagreements with HyperLeda could all be easily explained by the high quality of the multi-colour SDSS images, which allowed for a better detection of faint spiral structures. The ATLAS^{3D} sample of 260 ETGs obtained from this selection is given in Table 5 and illustrated in Fig. 5 and in Fig. 6, together with the HyperLeda morphological classification as provided by their T-type (E: $T \leq -3.5$; S0: $-3.5 < T \leq -0.5$; S0/a: $-0.5 < T \leq 0.5$).

3.2 Colour-magnitude diagram

The decision to select the ATLAS^{3D} sample based on morphology instead of colour was based on (i) the broad similarity of the two criteria, (ii) the non-availability of reliable colours for the whole parent sample and (iii) the robustness of morphology, as opposed to colours, against dust extinction. Still, we expect the ATLAS^{3D} sample to include mainly galaxies on the red sequence in a colour-magnitude diagram. This is verified in Fig. 7. The ATLAS^{3D} sample indeed defines a narrow colour-magnitude sequence approximated, in SDSS magnitudes, by

$$u - r = 2.53 - 0.097 \times (M_r + 20). \quad (5)$$

As found by previous authors there is little scatter in the relation at the high-mass end, while at the lower mass-end some galaxies appear to be still in transition between the blue and red sequence (Strateva et al. 2001; Conselice 2006; van den Bergh 2007; Bernardi et al. 2010). The 31 ETGs with SDSS colour and defined as slow rotators in Paper III all lie close to the red sequence with an rms scatter of 0.13 mag from the best-fitting relation. All the deviants ETGs are classified as fast rotators in Paper III. The nature of these objects will be investigated in detail in subsequent papers of this series. Spiral galaxies span the full region of the diagram, both on the red sequence and the the blue clouds, as found by previous studies.

4 SAURON DATA FOR THE ATLAS^{3D} SURVEY

4.1 Observing strategy

The main aim of the SAURON (Bacon et al. 2001) observations of the ATLAS^{3D} sample is to obtain global galaxy quantities like the specific stellar angular momentum λ_R, the $(V/\sigma, \varepsilon)$ the global kinematical misalignment, the luminosity-weighted second moment σ_e, the stellar and total mass-to-light ratio, the mean stellar population and the ionized gas emission. To be representative of the galaxies as a whole, these quantities need to be measured at least within one projected half-light radius R_e. Moreover for a given observed area, more accurate values of the kinematical quantities are

Figure 6. Same as in Fig. 5 for the fast rotators ETGs in the ATLAS^{3D} sample, sorted by increasing λ_R. The first panel contains mostly round objects. Many of them are barred (Paper II), nearly face-on, S0 galaxies and often contain stellar rings (e.g. NGC4608), while others appears face-on from the geometry of their dust. This suggests that the round shape and low λ_R of these objects is not intrinsic, but due to their low inclination ($i = 90^\circ$ being edge on). On the contrary the last panel is dominated by nearly edge-on disks, which explains their high λ_R.

Figure 6. — continued

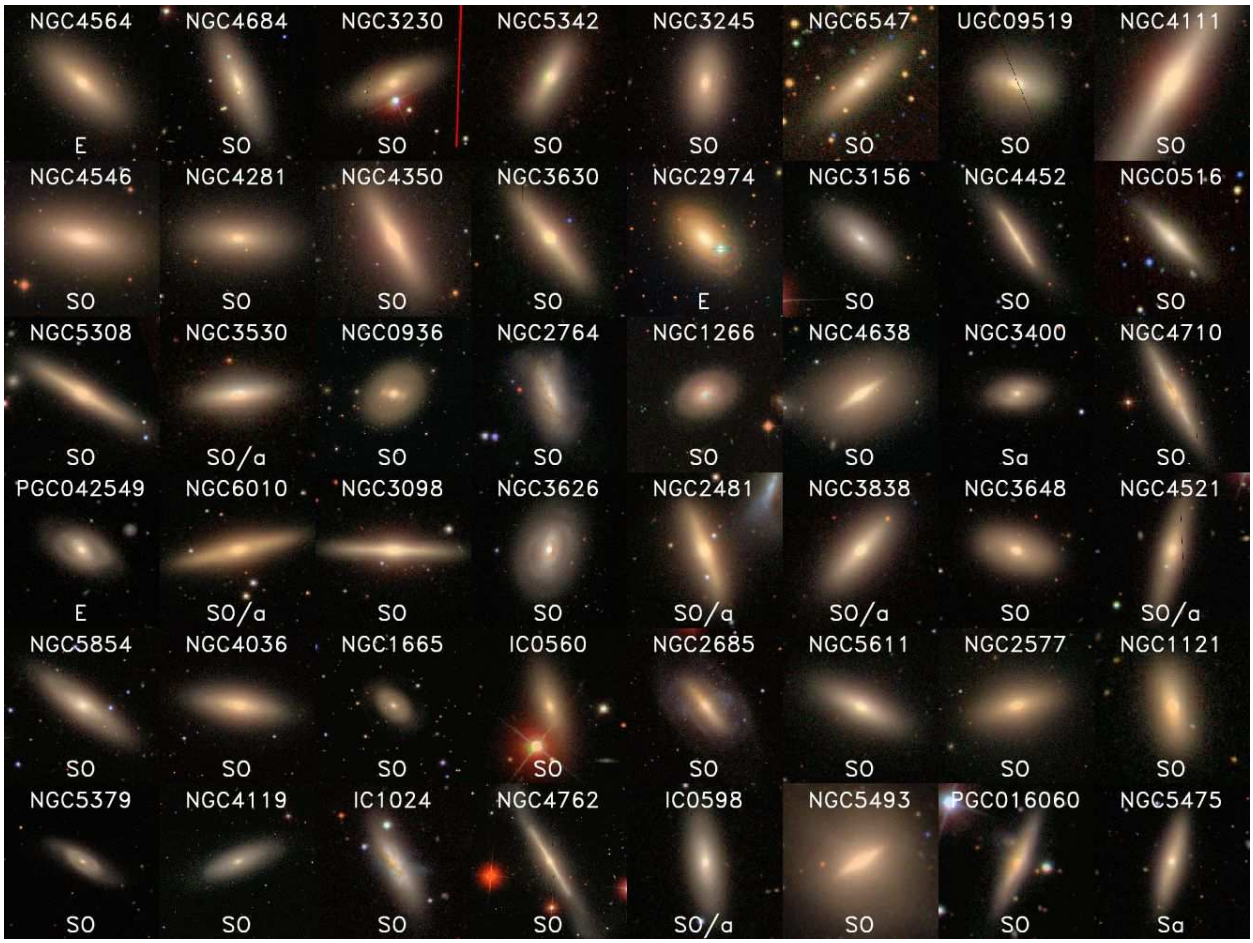

Figure 6. — continued

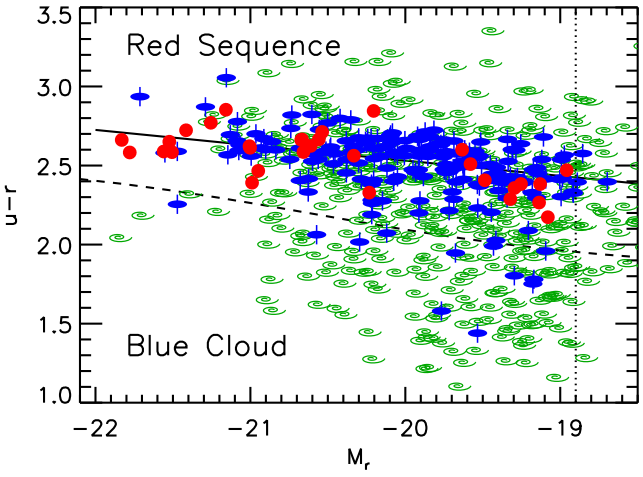

Figure 7. u-r versus M_r colour-magnitude diagram for the morphologically-selected ATLAS^{3D} parent sample with SDSS photometry. The blue ellipses with axis are fast-rotators ETGs, the red filled circles are slow rotators ETGs, while the green spirals are spiral galaxies. The dashed line indicates the separation between red sequence and blue cloud established by Baldry et al. (2004, 2006), from a sample of 151,642 galaxies. The vertical dotted line indicates our approximate survey completeness limit in r-band $M_r \lesssim -18.9$ mag. The solid line is a linear robust fit to the ETGs only, minimizing the sum of the absolute residuals.

obtained when the quantities are measured within ellipses instead of circles, with ellipticity given by the galaxy photometry and the position angle defined by the stellar kinematics (see appendix B of Cappellari et al. 2007). In addition, when galaxies are barred, the SAURON survey has shown that the kinematics are generally still aligned with the position angle of the galaxy photometry at large radii $\mathrm{PA_{phot}}$ (Krajnović et al. 2008), which defines the position of the line-of-nodes of the disk. These requirements, which derive from our experience with the SAURON survey (de Zeeuw et al. 2002), lead to the following optimized observing strategy, which we systematically applied for the SAURON observation of the ATLAS^{3D} sample:

(i) When $R_e \leq 30''$ take a single SAURON field and orient the SAURON major axis with the large radii $\mathrm{PA_{phot}}$;

(ii) When $R_e > 30''$ then we take a mosaic of two SAURON fields. Given the size of the SAURON field of $33'' \times 41''$, the criterion of maximizing the area of the largest isophote, of axial ratio q', enclosed within the observed field-of-view, becomes:

(a) If $q' < 0.55$ the SAURON long axis is aligned with $\mathrm{PA_{phot}}$ and the mosaic is made by matching the two SAURON pointings along the short side;

(b) If $q' \geq 0.55$ the SAURON short axis is aligned with $\mathrm{PA_{phot}}$ and the mosaic is made by matching the two SAURON pointings along the long side;

At the time of the SAURON observations the only photometry available to us for the whole sample was from 2MASS. We adopted the R_e provided by the 2MASS XSC, which is determined via growth curves within elliptical apertures. Specifically, in terms of the XSC catalogs parameters, we defined

$$R_e{}^{2MASS} = \mathrm{MEDIAN}(\mathrm{j\_r\_eff}, \mathrm{h\_r\_eff}, \mathrm{k\_r\_eff}) \times \sqrt{\mathrm{k\_ba}}, \quad (6)$$

as the median of the three 2MASS values in the J, H and K_s-band, where the factor $\sqrt{\mathrm{k\_ba}}$ takes into account the fact that the 2MASS values are the semi-major axes of the ellipses enclosing half of the galaxy light and we want the radius of the circle with the same area. This $R_e{}^{2MASS}$ was compared to the $R_e{}^{RC3}$ provided by the RC3 catalogue and measured via growth curves within circular apertures. The two values correlate well, with an observed rms scatter of 0.12 dex in R_e, which implies an error of about 22% in each R_e determination (assuming they have similar errors). However there is a general offset by a factor $R_e{}^{RC3} \approx 1.7 \times R_e{}^{2MASS}$ between the two determinations (Fig. 8). The rms scatter in the $R_e{}^{RC3} - R_e{}^{2MASS}$ correlation is close to the one (0.11 dex) we obtain when comparing $R_e{}^{RC3}$ to 46 values determined using growth curves in the I-band for the SAURON survey (Cappellari et al. 2006; Kuntschner et al. 2006). In that case however the offset in the values is negligible (factor 0.95). We conclude that the 2MASS R_e determinations have comparable accuracy to the RC3 and SAURON determination, when they are increased by a factor 1.7 to account for the differences in the observed photometric band and in the depth of the photometry data. All three values are consistent with having a similar error of $\approx 22\%$ in R_e. This rather large error is consistent with the findings of Chen et al. (2010) from another extensive comparison of R_e values. To further improve the accuracy we adopted $R_e = (1.7 \times R_e{}^{2MASS} + R_e{}^{RC3})/2$ for the 412/871 galaxies with both 2MASS and RC3 determinations and $R_e = 1.7 \times R_e{}^{2MASS}$ when only 2MASS was available. The values of R_e for the full parent sample, divided into ETGs and spirals, are given in Table 5 and Table 6.

4.2 Integral-field spectroscopic observations

The SAURON integral-field spectrograph was first mounted at the William Herschel Telescope (WHT) at the Observatory of El Roque des Los Muchachos on La Palma in 1999. It has been used extensively in particular in the course of the SAURON survey, but also in separate smaller efforts (e.g. Bower et al. 2004; Allard et al. 2005; Dumas et al. 2007; Weijmans et al. 2010). Given that the ATLAS^{3D} selection criteria are by design very similar to the ones in the SAURON survey, a total of 64 ETGs had been observed before the beginning of the ATLAS^{3D} observing campaign. 49 ETGs were part of the main survey (de Zeeuw et al. 2002), out of which 47 were presented in the sub-sample of ETGs (Emsellem et al. 2004) and two in the early-spirals sub-sample (Falcón-Barroso et al. 2006). 14 'special' ETGs within the ATLAS^{3D} volume had been observed with SAURON in the course of other projects (table 3 of Cappellari et al. 2007). All these galaxies were observed before the volume phase holographic (VPH) grating came into use and were taken with an exposure time of 2 hours on source, in some cases with multiple spatial pointings to cover galaxies to roughly one effective (projected half-light R_e) radius. All the observations were obtained in the low spatial resolution mode in which the instrument has a field-of-view of $33'' \times 41''$ sampled with $0\farcs94$ square lenslets and with a spectral resolution of 4.2 Å FWHM ($\sigma_{\rm instr} = 105$ km s^{-1}), covering the wavelength range 4800–5380 Å.

To observe the additional 196 galaxies we were allocated 38

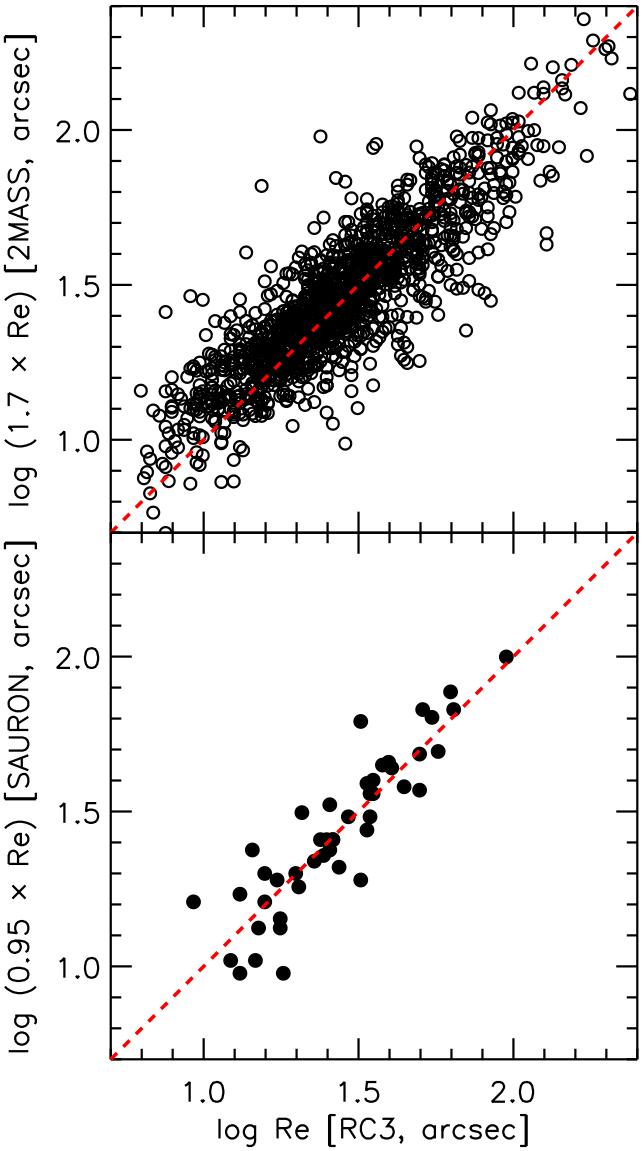

Figure 8. Testing the accuracy of R_e determinations. *Top Panel:* Comparison between 1353 values of R_e given by RC3 and the ones given by 2MASS (computed as described in the text), scaled by the best-fitting factor of 1.7. *Bottom Panel:* Same as in the top panel for the RC3 R_e and the ones for 46 ETGs of the SAURON survey. Once corrected for systematic differences, all three R_e determinations are consistent with a similar error of $\approx 22\%$.

Table 3. SAURON observing runs for the ATLAS^{3D} sample

Run	Dates	Clear
1	2007 April 10–23	12/14
2	2007 August 13–15	3/3
3	2008 January 9–15	6/7
4	2008 February 27 – March 11	11/14

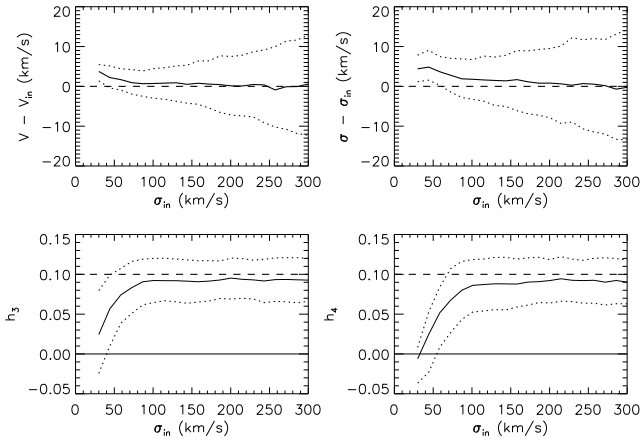

Figure 9. Testing penalization in pPXF. We simulated spectra with the $S/N = 40$ of our data and an LOSVD with $h_3 = 0.1$, $h_4 = 0.1$ and σ in the range between 30 and 300 km s^{-1}. We extracted the kinematics with pPXF and a penalty $\lambda = 0.5$. The lines in the top two panels show the 50th (median, solid line), 16th and 84th percentiles (1σ errors, dotted lines) of the differences between the measured values and the input values of the mean velocity $V_{\rm in}$ and the velocity dispersion $\sigma_{\rm in}$. The bottom panels show the same lines for the recovered values of h_3 and h_4, compared to the input values (dashed line). The h_3 and h_4 parameters can only be recovered when $\sigma_{\rm in} \gtrsim 100$ km s^{-1}. Typical statistical errors in the kinematics parameter for $\sigma_{\rm in} \approx 200$ km s^{-1} are 6 km s^{-1}, 7 km s^{-1}, 0.03 and 0.03, for V, σ, h_3 and h_4 respectively.

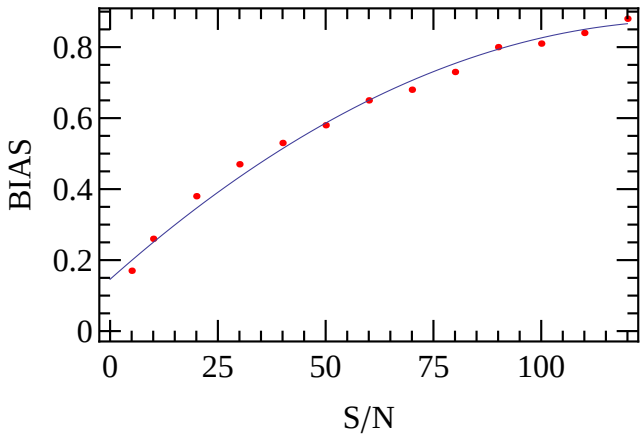

Figure 10. Relation between the S/N of the SAURON spectrum and the optimal penalty parameter λ (keyword BIAS) in pPXF. The solid line is the polynomial BIAS $= 0.15 + 0.0107\ S/N - 0.00004\ (S/N)^2$

observing nights comprising four observing runs spread over three consecutive semesters as part of a long-term project at the WHT (Table 3). The time allocation was split equally between Dutch and UK time. We had excellent weather with just 16% of nights lost due to clouds, compared to a normal average for the period of around 30%. This fact, combined with an efficient observing strategy allowed us to complete all observations of the ATLAS$^{\rm 3D}$ sample galaxies in the allocated time.

The optimal scheduling of the observations of the 196 galaxies, in some cases using multiple spatial pointings, was performed with a dedicated IDL script which gave higher priority to the intrinsically brightest galaxies, took into account the galaxy coordinates, the need for multiple pointings, the dates of the four observing runs, and the moon position and phase. The script could be easily re-run to modify the scheduling to account for time lost due to bad weather. The observations were performed with the VPH grating, which provides a resolution of 3.9 Å FWHM ($\sigma_{\rm instr} = 98$ km s^{-1}), about 7% better than for the SAURON survey. The adopted on-source exposure time was 1 hour, split into two equal 30 min exposure dithered by a couple of arcseconds.

4.3 Data reduction and stellar kinematics extraction

The SAURON data reduction followed standard procedures and used the dedicated XSAURON software developed at Centre de Recherche Astronomique de Lyon (CRAL) and was already described in Bacon et al. (2001) and Emsellem et al. (2004). However some details of our approach have been improved after the original publication of the data. For this reason we re-extracted all the stellar kinematics using the improved and completely homogeneous approach for the entire ATLAS$^{\rm 3D}$ dataset. We describe here the minor differences with respect to what was published before.

The data were spatially binned with the adaptive Voronoi method[8] of Cappellari & Copin (2003), which optimally solves the problem of preserving the maximum spatial resolution of two-dimensional data, given a constraint on the minimum signal-to-noise ratio (S/N). We adopted a target $S/N = 40$ for all the data used in the ATLAS$^{\rm 3D}$ survey, including the previous SAURON observations, which were re-extracted adopting for consistency this lower S/N instead of the $S/N = 60$ as originally published in Emsellem et al. (2004).

The stellar kinematics were extracted with the penalized pixel-fitting (pPXF) software[8] (Cappellari & Emsellem 2004), which simultaneously fits the stellar kinematics and the optimal linear combination of spectral templates to the observed spectrum, using a maximum-likelihood approach to suppress noisy solutions. The line-of-sight velocity distribution (LOSVD) is described via the Gauss-Hermite parametrization up to $h_3 - h_4$ (van der Marel & Franx 1993; Gerhard 1993). We employed as stellar template an optimal linear combination of stars from the MILES library[9] (Sánchez-Blázquez et al. 2006), which was separately determined for every galaxy. We did not allow the template to change in every bin, to eliminate small artifacts in the kinematics due imperfections in the velocity alinement of the MILES stars. We adjusted the penalty in pPXF to a value $\lambda = 0.5$, optimized for the adopted S/N. Following the pPXF documentation we determined the optimal λ by requiring the maximum bias in the Gauss-Hermite parameters h_3 and h_4 to be equal to rms/3, where the rms is the scatter of the measurements obtained from a Monte Carlo simulations with the adopted $S/N = 40$ and a well resolved stellar dispersion $\sigma \gtrsim 180$ km s^{-1} (Fig. 9). In a handful of cases we could not reach the required S/N without employing excessively large Voronoi bins. In those cases we further reduced the target S/N. For those galaxies we correspondingly adapted the penalty in pPXF according to the empirical relation of Fig. 10. For usage in cases where we need to approximate the stellar velocity second moments and not the full LOSVD — e.g. to fit models based on the Jeans (1922) equations or measure λ_R or V/σ — we separately extracted the kinematics assuming a simple Gaussian LOSVD. In that case the pPXF penalty is ignored. In all cases the errors on the kinematics were determined via bootstrapping (Efron & Tibshirani 1993),

[8] Available from http://purl.org/cappellari/idl
[9] Available from http://miles.iac.es/

by randomly re-sampling the pPXF fit residuals of the best fit and repeating the kinematic fit for 100 realizations, with a zero penalty (see Sec. 3.4 of Cappellari & Emsellem 2004). The homogeneous set of integral-field SAURON kinematics introduced in this paper, together with the stellar population parameters, the characteristics of the ionized gas and the entire data cubes for the full ATLAS^{3D} sample will be made available via the project Web page[10] at the end of our project.

As discussed in detail in Cappellari & Emsellem (2004) and illustrated in Fig. 9, the SAURON spectroscopic data allow the extraction of the full stellar Line-of-Sight Velocity-Distribution (LOSVD), including the Gauss-Hermite parameters, only for observed velocity dispersions $\sigma \gtrsim 120$ km s^{-1}. Below this value the h_3 and h_4 start becoming unconstrained by the data, due to the spectral under-sampling and for this reason the pPXF method automatically and gradually penalizes them towards zero to keep the noise on the mean velocity V and velocity dispersion σ under control. As the minimum S/N of our data is defined by our Voronoi binning criterion, the degree of penalization depends only on σ as illustrated in the Monte Carlo simulation of Fig. 9. This effect is also illustrated for ATLAS^{3D} data in Fig. 11, for a small set of galaxies with a range of luminosity-weighed σ_e within 1Re (defined as in Cappellari et al. 2006). The figure shows the range of data quality for the stellar kinematical data for the ATLAS^{3D} survey. At high σ_e the data have a quality which is comparable to the one for the SAURON survey presented in Emsellem et al. (2004). The shorter exposure time of the ATLAS^{3D} survey is in part compensated by the use of the VPH grating and in part by the adoption of larger Voronoi bins. However at $\sigma_e \lesssim 120$ km s^{-1} there is not enough information in the data to constrain h_3 and h_4. Contrary to the SAURON survey the volume-limited ATLAS^{3D} survey is dominated by the more common low-luminosity galaxies, which also tend to have low dispersion. In practice we find that $\approx 40\%$ of the galaxies in the sample have $\sigma_e \lesssim 120$ km s^{-1} and for those objects we can only recover reliable V and σ values. Although the kinematics are not sufficient to constrain general dynamical models for the full sample, they still provide very reliable global values of specific angular momenta and galaxy masses for all galaxies (e.g. Cappellari et al. 2010).

We also used the SAURON stellar kinematic to measure extremely robust heliocentric recession velocities $V_{\rm hel}$ for all galaxies in the sample. Repeated determinations indicate an 1σ accuracy $\Delta V_{\rm hel} \approx 5$ km s^{-1}. The values were derived from the integral-field stellar kinematics by finding the value which needs to be subtracted from the observed velocity field to best fit a bi-anti-symmetric version of the velocity field[11]. This technique does not suffer from the uncertainties due to the slit centering, which affects spectroscopic surveys, or from the possibility of the gas not being associated to the galaxy, which affects H I determinations. The observed velocities were converted into velocities $V_{\rm hel}$ relative to the barycenter of the Solar System via the IDL routine `baryvel`, which implements the algorithm by Stumpff (1980) and is part of the IDL Astronomy User's Library (Landsman 1993). The measured $V_{\rm hel}$ values are given in Table 5.

[10] http://purl.org/atlas3d

[11] This was performed with the IDL routine FIT_KINEMATICS_PA described in Appendix C of Krajnović et al. (2006) and available here http://purl.org/cappellari/idl.

5 ADDITIONAL ATLAS^{3D} DATA AND SIMULATIONS

5.1 H I, CO and optical observations

Apart from the SAURON integral-field spectroscopic observations presented in detail in Section 4, the ATLAS^{3D} survey includes other multi-wavelength observations obtained with different instruments and facilities. These datasets will be presented in subsequent papers, however a summary of the main ones is presented in Table 4, and more information are given below:

(i) H I **interferometry:** We have observed the H I properties of all galaxies in the ATLAS^{3D} sample above $\delta = 10^\circ$ (due to the telescope latitude). This sub-sample includes 170 galaxies — 43 inside and 127 outside the Virgo cluster. We observed all galaxies outside Virgo, and galaxies inside Virgo detected by the Alfalfa survey (Giovanelli et al. 2005), with the Westerbork Synthesis Radio Telescope (WSRT). Some of the galaxies were observed with the WSRT as part of previous studies (Morganti et al. 2006; Józsa et al. 2009; Oosterloo et al. 2010). The integration time for all galaxies observed with the WSRT is 12 h, providing H I cubes at a resolution of ~ 30 arcsec and 16 km/s over a field of view of ~ 1 deg^2 and a velocity range of ~ 4000 km/s. We detect H I gas down to a column density of a few times 10^{19} cm^{-2}. The upper limits on M(H I) derived from these data ranges between 10^6 and a few times 10^7 $M_\odot$ depending on galaxy distance. This is typically ~ 5 times lower than upper limits derived from Alfalfa spectra. These observations and a discussion of the H I properties will be presented in Serra et al. (in preparation). Interesting objects, like extended disks, have been followed-up for deeper H I observations.

(ii) **CO single-dish:** All of the ATLAS^{3D} galaxies have been searched for ^{12}CO J=1-0 and 2-1 emission with the IRAM 30m telescope, including 204 new observations with the remainder collected from the recent literature. The data consist of a single pointing at the galaxy center, covering a bandwidth of 1300 km s^{-1} centered on the optical velocity. The rms noise levels of the 1-0 spectra are 3 mK (T_A^*) or better after binning to 31 km s^{-1} channels, so that the 3σ upper limit for a sum over a 300 km s^{-1} linewidth corresponds to a H_2 mass $\sim 1 \times 10^7$ M$_\odot$ for the most nearby sample members and $\sim 1 \times 10^8$ M$_\odot$ for the most distant members. A detailed description of the observations and the corresponding measurements are presented in Paper IV.

(iii) **CO interferometry:** The brighter CO detections have been, observed in the 1-0 line with the BIMA, Plateau de Bure, and CARMA millimeter interferometers in order to map the distribution and kinematics of the molecular gas. These observations are designed to provide the molecular surface densities and angular momenta for 80% of all of the molecular gas found in the ATLAS^{3D} sample, typically at resolutions of $5''$. Some additional data at higher and lower resolutions are obtained as necessary to probe the structure of the gas and recover the bulk of the emission detected in the single dish data. On-source integration times range from 4 to 20 hours and are also adjusted as necessary for high quality detections. A detailed description of the observations and the corresponding measurements are presented in Alatalo et al. (in preparation).

(iv) **INT optical imaging:** Observations with the Wide-Field Camera (WFC) at the 2.5m Isaac Newton Telescope (INT) were carried out to obtain u, g, r, i and z-band imaging for galaxies not observed by the SDSS. Images were taken through the 5 filters for 55 galaxies from the ATLAS^{3D} sample. Integration times were typically 60 to 160 seconds reaching sensitivities comparable or deeper than the SDSS. Galaxies already observed by SDSS were

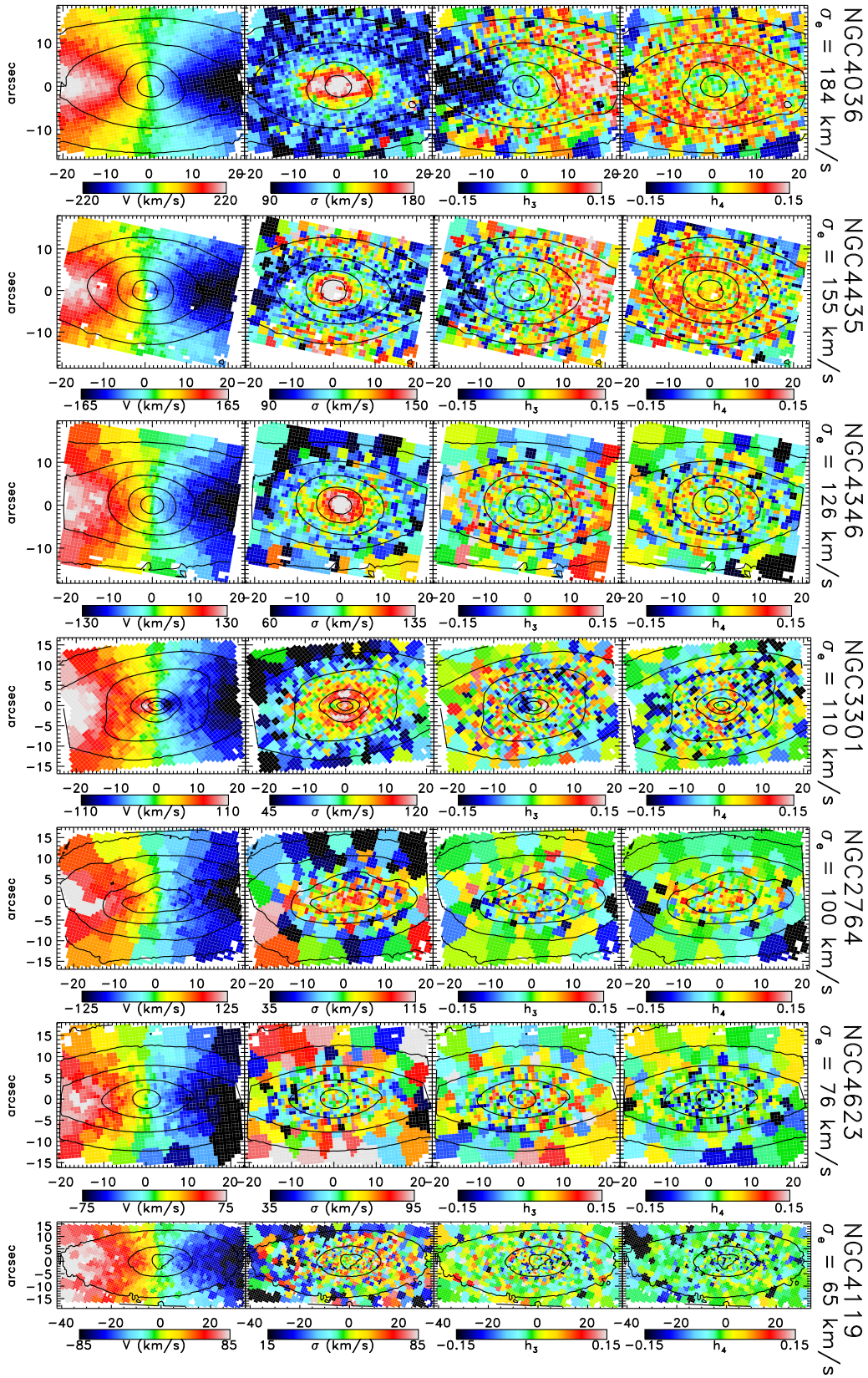

Figure 11. Quality of the SAURON kinematics in the ATLAS^{3D} survey. In each column from left to right shows the Voronoi binned kinematic moments extracted via pPXF from the SAURON data: mean velocity, V, velocity dispersion, σ, and higher Gauss-Hermite moments, h_3 and h_4. From top to bottom the data for seven newly-observed fast-rotators in the ATLAS^{3D} sample are sorted according to the luminosity-weighted dispersion σ_e within $1R_e$. Below $\sigma_e \lesssim 120$ km s^{-1} the data have insufficient information to constrain the full LOSVD and the Gauss-Hermite moments are automatically and gradually suppressed by pPXF towards zero to reduce the noise in V and σ, which can still be reliably recovered. About 40% of the galaxies in the sample have $\sigma_e \lesssim 120$ km s^{-1}.

Table 4. Multiwavelength ATLAS^{3D} data

Instrument	Tracer/Band/Res.	Number of Objects	Selection	Reference	Time Allocation
WSRT	H I @ 21 cm	170	$\delta > 10^\circ$	Serra et al. in preparation	1212 h
IRAM 30m	^{12}CO J=1-0 and 2-1	259	All	Paper IV	211 h
CARMA	^{12}CO J=1-0	32	$f > 19$ Jy km s^{-1}	Altalo et al. in preparation	467 h
INT + SDSS	u, g, r, i, z	35 + 225	All	Scott et al. in prep. + Abazajian et al. (2009)	5 n
SAURON	480–538 nm; $R = 1300$	260	All	This paper	38 n

observed in the runs as a cross-check in general and to bring the INT imaging onto the same photometric system as SDSS in particular. The images have been reduced and calibrated using the Astro-WISE system (Valentijn et al. 2007). A detailed description of the observations and the corresponding measurements are presented in Scott et al. (in preparation).

(v) **Targeted follow-ups:** We are also obtaining data for targeted subsets of the sample: Deep optical images of ATLAS^{3D} galaxies were obtained with the MegaCam camera installed on the Canada-France-Hawaii Telescope. This imaging part of the project aims to reach surface-brightness limits as low as 28.5 mag arcsec^2 in the g-band. Reaching such values allows to disclose very faint, diffuse structures in the outskirts of the ETGs, such as shells and tidal tails, that tell about their past mass accretion history. We have also started an observing campaign to obtain stellar kinematics and absorption line strengths out to large radii ($3 - 5R_e$) with IFUs (e.g. SAURON, VIRUS-P) for a number of ATLAS^{3D} galaxies. Following the methods outlined in Weijmans et al. (2009) we will construct dynamical models to trace the halo mass profiles. We primarily target galaxies that have been detected in H I to have a regularly rotating disc and ring, so that the H I kinematics can be added to the dynamical modeling.

5.2 Numerical simulations

The ATLAS^{3D} project includes a theoretical effort to interpret the observations using models of galaxy formation. We are attacking the problem via three parallel approaches as described below:

(i) **Binary mergers:** An extensive set of "idealized" (i.e. without the cosmological context) numerical simulations is being conducted. These simulations have been made at an unmatched resolution (softening length of 58 pc and a total number of particles of 1.2×10^7) with the goal to better understand the role of mergers in the formation and evolution of galaxies of the red sequence and to understand in details the physical processes involved during a merger (e.g. the formation of the Kinematically Decoupled Components, the energy and angular momentum exchanges). These simulations are also a powerful tool to perform direct comparisons with observations such as e.g., the morphology via the ellipticity, the kinematics via λ_R, the redistribution of the gas at large scales, the metallicity gradients and the Mg b – V_{esc} relation (Davies et al. 1993; Scott et al. 2009). The detailed description of the simulations and their associated results are presented in Bois et al. (2010) and Paper VI. Other idealized simulations of ATLAS^{3D} galaxies are performed with the RAMSES high-resolution grid-based hydrodynamical code (Teyssier 2002). Following the technique developed in Bournaud et al. (2010), we model the dynamics of atomic and molecular gas disks in early-type galaxies with parsec-scale resolution, based on accurate mass models extracted from the ATLAS^{3D} data. These models aim at understanding the dynamics, stability and star formation activity of the ISM in ETGs.

(ii) **Semi-analytic modeling:** In a second strand of simulations we address the formation of elliptical galaxies within a large scale cosmological setting using a semi-analytic modeling (SAM) approach. Using the knowledge gained from idealized high-resolution simulations of mergers and the formation of a limited number of cosmologically simulated ETGs we test formation scenarios within our SAM making full use of the completeness of the ATLAS^{3D} sample. The SAM we use is an extension of earlier work by Khochfar & Burkert (2005) and Khochfar & Silk (2006). Within the SAM we follow the individual history of a large statistical sample of galaxies to the present day, taking into account their merging history and physical processes related to e.g. gas cooling or star formation. In addition the SAM is used to make predictions on the evolution of these classes of ETGs, that can be tested with future observations (Khochfar et al in prep.).

(iii) **Cosmological simulations:** We will also make use of high resolution simulations of individual galaxies in a full cosmological context (i.e. Naab et al. 2007, 2009) to investigate the physical processes setting the present day kinematical properties of ETGs. We will use a new sample of simulations (Oser et al. 2010) covering the full mass range of the ATLAS^{3D} galaxies. From these simulated galaxies we will construct two-dimensional kinematical maps (Jesseit et al. 2007) to compare directly to the ATLAS^{3D} observations. The use of cosmological simulations is advantageous as we can link the present day properties to the evolutionary history embedded in the favored cosmology. We will also be able to investigate the influence of the merging history, dark matter and various feedback mechanisms on kinematic properties and the stellar populations.

6 SUMMARY

We described the motivation and goals of the ATLAS^{3D} project, which aims at constraining models of galaxy formation by obtaining two-dimensional observations of the distribution and kinematics of the atomic (H I), molecular (CO) and ionized gas, together with the stellar population and kinematics, for a volume-limited nearly mass-selected (K_s-band) sample of ETGs.

We defined the selection criteria for the volume-limited (1.16×10^5 Mpc^3) *parent* sample of 871 galaxies with $D < 42$ Mpc and $M_K < -21.5$ mag, satisfying our observability criteria, and investigated possible selection biases, especially due to redshift incompleteness. We found that incompleteness cannot amount to more than a couple of percent, making the sample essentially complete and representative of the nearby population. We additionally tested the representativeness of the sample by comparing its K_s-band luminosity function with the one derived from a much larger sample (Bell et al. 2003) and found a very good agreement. We de-

scribed the morphological selection used to extract the 260 ETGs of the ATLAS^{3D} sample from the parent sample and showed that the ETGs define a narrow red-sequence, on a colour-magnitude diagram, with few objects in transition from the blue cloud. We presented the size-luminosity relation for the ATLAS^{3D} sample and the full parent sample to illustrate the general characteristic of our galaxies.

We described the strategy for the SAURON integral-field observations, the data reduction, the extraction of the stellar kinematics and their typical errors. We gave an overview of the additional dataset already available for our sample, which include interferometric observations of the atomic gas as traced by H I, single-dish and interferometric observations of molecular gas as traced by the CO lines, and multi-band optical photometry. We summarized the ongoing semi-analytic modeling and the cosmological and binary-merger N-body simulations we are performing to interpret our observations.

This is the first paper of a series devoted to our understanding of the formation of ETGs. Key additional elements are provided by the kinematics, ages and chemical composition of the stars in the galaxies, the presence of cold atomic or molecular gas, the photometric profiles and the dynamical masses, as a function of environment. The observations for the ATLAS^{3D} sample will be compared against the model predictions, to test formation scenarios and to tune the model parameter. This will be the topic of future papers of this series. The ATLAS^{3D} project aims to constitute a zero redshift baseline, against which one can investigate the evolution of galaxy global parameters with redshift, to trace galaxy evolution back time. Future studies should extend this effort to more dense environment than can be explored in the nearby universe, and to increasingly higher redshifts to explore the time evolution of the structure of ETGs.

ACKNOWLEDGEMENTS

We thank the anonymous referee for a useful report. MC acknowledges support from a STFC Advanced Fellowship PP/D005574/1 and a Royal Society University Research Fellowship. This work was supported by the rolling grants 'Astrophysics at Oxford' PP/E001114/1 and ST/H002456/1 and visitors grants PPA/V/S/2002/00553, PP/E001564/1 and ST/H504862/1 from the UK Research Councils. RLD acknowledges travel and computer grants from Christ Church, Oxford and support from the Royal Society in the form of a Wolfson Merit Award 502011.K502/jd. RLD also acknowledges the support of the ESO Visitor Programme which funded a 3 month stay in 2010. SK acknowledges support from the the Royal Society Joint Projects Grant JP0869822. RMcD is supported by the Gemini Observatory, which is operated by the Association of Universities for Research in Astronomy, Inc., on behalf of the international Gemini partnership of Argentina, Australia, Brazil, Canada, Chile, the United Kingdom, and the United States of America. TN and MBois acknowledge support from the DFG Cluster of Excellence 'Origin and Structure of the Universe'. MS acknowledges support from a STFC Advanced Fellowship ST/F009186/1. NS and TD acknowledge support from an STFC studentship. The authors acknowledge financial support from ESO. We acknowledge the usage in pPXF of the MPFIT routine by Markwardt (2009). The SAURON observations were obtained at the William Herschel Telescope, operated by the Isaac Newton Group in the Spanish Observatorio del Roque de los Muchachos of the Instituto de Astrofisica de Canarias. We are grateful to the ING staff for their excellent support and creativity in quickly solving technical problem during the SAURON runs. We are grateful to Jesús Falcon-Barroso for useful discussions and help with the observations. MC is grateful to the NED staff for prompt support. This research has made use of the NASA/IPAC Extragalactic Database (NED) which is operated by the Jet Propulsion Laboratory, California Institute of Technology, under contract with the National Aeronautics and Space Administration. We acknowledge the usage of the HyperLeda database (http://leda.univ-lyon1.fr). Funding for the SDSS and SDSS-II was provided by the Alfred P. Sloan Foundation, the Participating Institutions, the National Science Foundation, the U.S. Department of Energy, the National Aeronautics and Space Administration, the Japanese Monbukagakusho, the Max Planck Society, and the Higher Education Funding Council for England. The SDSS was managed by the Astrophysical Research Consortium for the Participating Institutions. This publication makes use of data products from the Two Micron All Sky Survey, which is a joint project of the University of Massachusetts and the Infrared Processing and Analysis Center/California Institute of Technology, funded by the National Aeronautics and Space Administration and the National Science Foundation.

REFERENCES

Abazajian K. N., et al. 2009, ApJS, 182, 543
Allard E. L., Peletier R. F., Knapen J. H., 2005, ApJ, 633, L25
Bacon R., et al. 2001, MNRAS, 326, 23
Baldry I. K., Balogh M. L., Bower R. G., Glazebrook K., Nichol R. C., Bamford S. P., Budavari T., 2006, MNRAS, 373, 469
Baldry I. K., Glazebrook K., Brinkmann J., Ivezić Ž., Lupton R. H., Nichol R. C., Szalay A. S., 2004, ApJ, 600, 681
Barnes J. E., 1992, ApJ, 393, 484
Bell E. F., de Jong R. S., 2001, ApJ, 550, 212
Bell E. F., et al. 2003, ApJS, 149, 289
Bell E. F., et al. 2004, ApJ, 608, 752
Bender R., Burstein D., Faber S. M., 1992, ApJ, 399, 462
Bender R., Surma P., Doebereiner S., Moellenhoff C., Madejsky R., 1989, A&A, 217, 35
Bernardi M., Shankar F., Hyde J. B., Mei S., Marulli F., Sheth R. K., 2010, MNRAS, 404, 2087
Binney J., 1978, MNRAS, 183, 501
Blakeslee J. P., et al. 2010, ApJ, 724, 657
Blakeslee J. P., et al. 2009, ApJ, 694, 556
Bois M., et al. 2010, MNRAS, 406, 2405
Bois M., et al. 2011, MNRAS, submitted (Paper VI)
Bournaud F., Elmegreen B. G., Teyssier R., Block D. L., Puerari I., 2010, MNRAS, 409, 1088
Bournaud F., Jog C. J., Combes F., 2007, A&A, 476, 1179
Bower R. G., Benson A. J., Malbon R., Helly J. C., Frenk C. S., Baugh C. M., Cole S., Lacey C. G., 2006, MNRAS, 370, 645
Bower R. G., et al. 2004, MNRAS, 351, 63
Cappellari M., et al. 2006, MNRAS, 366, 1126
Cappellari M., Copin Y., 2003, MNRAS, 342, 345
Cappellari M., Emsellem E., 2004, PASP, 116, 138
Cappellari M., et al. 2007, MNRAS, 379, 418
Cappellari M., et al. 2011, MNRAS, submitted (Paper VII)
Cappellari M., et al. 2010, Highlights of Astronomy, 15, 81
Cattaneo A., Dekel A., Devriendt J., Guiderdoni B., Blaizot J., 2006, MNRAS, 370, 1651
Chen C., Côté P., West A. A., Peng E. W., Ferrarese L., 2010, ApJS, 191, 1

Cimatti A., et al., 2008, A&A, 482, 21
Cole S., et al. 2001, MNRAS, 326, 255
Conselice C. J., 2006, MNRAS, 373, 1389
Cox T. J., Dutta S. N., Di Matteo T., Hernquist L., Hopkins P. F., Robertson B., Springel V., 2006, ApJ, 650, 791
Crook J. R., et al. 2007, ApJ, 655, 790
Croton D. J., et al. 2006, MNRAS, 365, 11
Daddi E., et al. 2005, ApJ, 626, 680
Davies R. L., Efstathiou G., Fall S. M., Illingworth G., Schechter P. L., 1983, ApJ, 266, 41
Davies R. L., Sadler E. M., Peletier R. F., 1993, MNRAS, 262, 650
Davis T. A., et al. 2011, MNRAS, submitted (Paper V)
de Vaucouleurs G., 1959, Handbuch der Physik, 53, 311
de Vaucouleurs G., 1963, ApJS, 8, 31
de Vaucouleurs G., de Vaucouleurs A., Corwin Jr. H. G., Buta R. J., Paturel G., Fouque P., 1991, Third Reference Catalogue of Bright Galaxies. Volume 1-3, XII, 2069 pp. 7 figs.. Springer-Verlag Berlin Heidelberg New York
de Vaucouleurs G., de Vaucouleurs A., Corwin J. R., 1976, in Second reference catalogue of bright galaxies, 1976, Austin: University of Texas Press. Second reference catalogue of bright galaxies. pp 0–+
de Zeeuw P. T., et al. 2002, MNRAS, 329, 513
Dekel A., Birnboim Y., 2006, MNRAS, 368, 2
Di Matteo T., Springel V., Hernquist L., 2005, Nature, 433, 604
Djorgovski S., Davis M., 1987, ApJ, 313, 59
Dressler A., Lynden-Bell D., Burstein D., Davies R. L., Faber S. M., Terlevich R., Wegner G., 1987, ApJ, 313, 42
Dumas G., Mundell C. G., Emsellem E., Nagar N. M., 2007, MNRAS, 379, 1249
Dunkley J., et al. 2009, ApJS, 180, 306
Efron B., Tibshirani R., 1993
Emsellem E., et al. 2004, MNRAS, 352, 721
Emsellem E., et al. 2007, MNRAS, 379, 401
Emsellem E., et al. 2011, MNRAS, submitted (Paper III)
Faber S. M., et al. 1997, AJ, 114, 1771
Faber S. M., Jackson R. E., 1976, ApJ, 204, 668
Faber S. M., et al. 2007, ApJ, 665, 265
Falcón-Barroso J., et al. 2006, MNRAS, 369, 529
Ferrarese L., et al. 2006, ApJ, 644, L21
Ferrarese L., van den Bosch F. C., Ford H. C., Jaffe W., O'Connell R. W., 1994, AJ, 108, 1598
Gerhard O. E., 1993, MNRAS, 265, 213
Giovanelli R., et al. 2005, AJ, 130, 2598
Graham A. W., 2004, ApJ, 613, L33
Granato G. L., De Zotti G., Silva L., Bressan A., Danese L., 2004, ApJ, 600, 580
Hernquist L., 1992, ApJ, 400, 460
Hopkins P. F., Hernquist L., Cox T. J., Keres D., Wuyts S., 2009, ApJ, 691, 1424
Hubble E. P., 1936, Realm of the Nebulae. Yale Univ. Press, New Haven
Huchra J., Davis M., Latham D., Tonry J., 1983, ApJS, 52, 89
Huchra J. P., et al. 2005, in Colless M., Staveley-Smith L., Stathakis R., eds, Maps of the Cosmos Vol. 216 of IAU Symposium, 2MASS redshift survey. p. 170
Huchra J. P., Geller M. J., Clemens C. M., Tokarz S. P., Michel A., 1992, Bulletin d'Information du Centre de Donnees Stellaires, 41, 31
Illingworth G., 1977, ApJ, 218, L43
Jarrett T. H., Chester T., Cutri R., Schneider S., Skrutskie M., Huchra J. P., 2000, AJ, 119, 2498
Jeans J. H., 1922, MNRAS, 82, 122
Jeong H., Yi S. K., et al. 2009, MNRAS, 398, 2028
Jesseit R., Cappellari M., Naab T., Emsellem E., Burkert A., 2009, MNRAS, 397, 1202
Jesseit R., Naab T., Peletier R. F., Burkert A., 2007, MNRAS, 376, 997
Johansson P. H., Naab T., Ostriker J. P., 2009, ApJ, 697, L38
Józsa G. I. G., Oosterloo T. A., Morganti R., Klein U., Erben T., 2009, A&A, 494, 489
Karachentsev I. D., Nasonova O. G., 2010, MNRAS, 405, 1075
Kereš D., Katz N., Weinberg D. H., Davé R., 2005, MNRAS, 363, 2
Khochfar S., Burkert A., 2003, ApJ, 597, L117
Khochfar S., Burkert A., 2005, MNRAS, 359, 1379
Khochfar S., Ostriker J. P., 2008, ApJ, 680, 54
Khochfar S., Silk J., 2006, ApJ, 648, L21
Khochfar S., Silk J., 2009, MNRAS, 397, 506
Kochanek C. S., et al. 2001, ApJ, 560, 566
Kormendy J., Bender R., 1996, ApJ, 464, L119+
Kormendy J., Fisher D. B., Cornell M. E., Bender R., 2009, ApJS, 182, 216
Kormendy J., Richstone D., 1995, ARA&A, 33, 581
Krajnović D., et al. 2008, MNRAS, 390, 93
Krajnović D., Cappellari M., de Zeeuw P. T., Copin Y., 2006, MNRAS, 366, 787
Krajnović D., et al. 2011, MNRAS, submitted (Paper II)
Kuntschner H., et al. 2006, MNRAS, 369, 497
Kuntschner H., et al. 2010, ArXiv e-prints
Landsman W. B., 1993, in R. J. Hanisch, R. J. V. Brissenden, & J. Barnes ed., Astronomical Data Analysis Software and Systems II Vol. 52 of Astronomical Society of the Pacific Conference Series, The IDL Astronomy User's Library. pp 246–+
Lauer T. R., et al. 1995, AJ, 110, 2622
Lupton R., Blanton M. R., Fekete G., Hogg D. W., O'Mullane W., Szalay A., Wherry N., 2004, PASP, 116, 133
Maraston C., 2005, MNRAS, 362, 799
Markwardt C. B., 2009, in D. A. Bohlender, D. Durand, & P. Dowler ed., Astronomical Society of the Pacific Conference Series Vol. 411 of Astronomical Society of the Pacific Conference Series, Non-linear Least-squares Fitting in IDL with MPFIT. pp 251–+
McDermid R. M., et al. 2006, MNRAS, 373, 906
Mei S., et al. 2007, ApJ, 655, 144
Morganti R., et al. 2006, MNRAS, 371, 157
Mould J. R., et al. 2000, ApJ, 529, 786
Naab T., Burkert A., 2003, ApJ, 597, 893
Naab T., Burkert A., Hernquist L., 1999, ApJ, 523, L133
Naab T., Jesseit R., Burkert A., 2006, MNRAS, 372, 839
Naab T., Johansson P. H., Ostriker J. P., 2009, ApJ, 699, L178
Naab T., Johansson P. H., Ostriker J. P., Efstathiou G., 2007, ApJ, 658, 710
Naab T., Khochfar S., Burkert A., 2006, ApJ, 636, L81
Oosterloo T., et al. 2010, MNRAS, 409, 500
Oser L., Ostriker J. P., Naab T., Johansson P. H., Burkert A., 2010, MNRAS, submitted (arXiv:1010.1381)
Paturel G., Petit C., Prugniel P., Theureau G., Rousseau J., Brouty M., Dubois P., Cambrésy L., 2003, A&A, 412, 45
Perlmutter S., et al. 1999, ApJ, 517, 565
Press W. H., Teukolsky S. A., Vetterling W. T., Flannery B. P.,

1992, Numerical recipes in FORTRAN. The art of scientific computing. Cambridge: University Press, —c1992, 2nd ed.
Riess A. G., et al. 1998, AJ, 116, 1009
Robertson B., Bullock J. S., Cox T. J., Di Matteo T., Hernquist L., Springel V., Yoshida N., 2006, ApJ, 645, 986
Sánchez-Blázquez P., et al. 2006, MNRAS, 371, 703
Sandage A., 1961, The Hubble Atlas. Carnegie Institution, Washington
Sandage A., 1975, Classification and Stellar Content of Galaxies Obtained from Direct Photography. Galaxies and the Universe, p. 170
Sarzi M., et al. 2006, MNRAS, 366, 1151
Sarzi M., et al. 2010, MNRAS, 402, 2187
Schechter P., 1976, ApJ, 203, 297
Schlegel D. J., Finkbeiner D. P., Davis M., 1998, ApJ, 500, 525
Scott N., et al. 2009, MNRAS, 398, 1835
Sersic J. L., 1968, Atlas de galaxias australes. Cordoba, Argentina: Observatorio Astronomico, 1968
Shankar F., Bernardi M., 2009, MNRAS, 396, L76
Shapiro K. L., et al. 2010, MNRAS, 402, 2140
Shen S., Mo H. J., White S. D. M., Blanton M. R., Kauffmann G., Voges W., Brinkmann J., Csabai I., 2003, MNRAS, 343, 978
Skrutskie M. F., et al. 2006, AJ, 131, 1163
Spergel D. N., Bean R., Doré O., et al. 2007, ApJS, 170, 377
Springel V., Di Matteo T., Hernquist L., 2005, ApJ, 620, L79
Springel V., White S. D. M., Jenkins A., et al. 2005, Nature, 435, 629
Strateva I., Ivezić Ž., Knapp G. R., et al. 2001, AJ, 122, 1861
Stumpff P., 1980, A&A Supp. Ser., 41, 1
Taylor E. N., Franx M., Glazebrook K., Brinchmann J., van der Wel A., van Dokkum P. G., 2010, ApJ, 720, 723
Teyssier R., 2002, A&A, 385, 337
Tonry J. L., Dressler A., Blakeslee J. P., Ajhar E. A., Fletcher A. B., Luppino G. A., Metzger M. R., Moore C. B., 2001, ApJ, 546, 681
Trujillo I., Cenarro A. J., de Lorenzo-Cáceres A., Vazdekis A., de la Rosa I. G., Cava A., 2009, ApJ, 692, L118
Trujillo I., Feulner G., Goranova Y., et al. 2006, MNRAS, 373, L36
Tully R. B., Fisher J. R., 1977, A&A, 54, 661
Tully R. B., Rizzi L., Shaya E. J., Courtois H. M., Makarov D. I., Jacobs B. A., 2009, AJ, 138, 323
Tully R. B., Shaya E. J., Karachentsev I. D., Courtois H. M., Kocevski D. D., Rizzi L., Peel A., 2008, ApJ, 676, 184
Valentijn E. A., McFarland J. P., Snigula J., et al. 2007, in R. A. Shaw, F. Hill, & D. J. Bell ed., Astronomical Data Analysis Software and Systems XVI Vol. 376 of Astronomical Society of the Pacific Conference Series, Astro-WISE: Chaining to the Universe. pp 491
Valentinuzzi T., et al. 2010, ApJ, 712, 226
van den Bergh S., 2007, AJ, 134, 1508
van der Marel R. P., Franx M., 1993, ApJ, 407, 525
van der Wel A., Bell E. F., van den Bosch F. C., Gallazzi A., Rix H.-W., 2009, ApJ, 698, 1232
van Dokkum P. G., et al. 2008, ApJ, 677, L5
Weijmans A., Bower R. G., Geach J. E., Swinbank A. M., Wilman R. J., de Zeeuw P. T., Morris S. L., 2010, MNRAS, 402, 2245
Weijmans A., et al. 2009, MNRAS, 398, 561
York D. G., et al. 2000, AJ, 120, 1579
Young L. M., et al. 2011, MNRAS, submitted (Paper IV)

Table 5. The ATLAS^{3D} sample or 260 early-type (E and S0) galaxies

Galaxy	RA (deg)	DEC (deg)	SBF	NED-D	Virgo	$V_{\rm hel}$ (km s^{-1})	D (Mpc)	M_K (mag)	A_B (mag)	T-type	$\log R_{\rm e}$ ($''$)
(1)	(2)	(3)	(4)	(5)	(6)	(7)	(8)	(9)	(10)	(11)	(12)
IC0560	146.472656	-0.268221	0	0	0	1853	27.2	-22.10	0.59	-0.7	1.11
IC0598	153.202423	43.145546	0	0	0	2256	35.3	-22.60	0.06	-0.1	1.02
IC0676	168.165909	9.055736	0	0	0	1429	24.6	-22.27	0.11	-1.3	1.35
IC0719	175.077042	9.009861	0	0	0	1833	29.4	-22.70	0.22	-2.0	1.10
IC0782	185.404053	5.765672	0	0	0	2424	36.3	-22.02	0.09	2.7	1.35
IC1024	217.863419	3.009107	0	0	0	1479	24.2	-21.85	0.13	-2.0	1.05
IC3631	189.950195	12.973927	0	0	0	2822	42.0	-22.01	0.17	-1.3	1.13
NGC0448	18.818876	-1.626105	1	1	0	1908	29.5	-23.02	0.26	-2.5	1.05
NGC0474	20.027901	3.415270	0	1	0	2315	30.9	-23.91	0.15	-2.0	1.52
NGC0502	20.731415	9.049169	0	0	0	2524	35.9	-23.05	0.17	-2.0	1.07
NGC0509	20.850327	9.433469	0	0	0	2261	32.3	-21.89	0.20	-1.3	1.37
NGC0516	21.033607	9.551668	0	0	0	2437	34.7	-22.21	0.29	-1.5	1.16
NGC0524	21.198778	9.538793	1	10	0	2403	23.3	-24.71	0.36	-1.2	1.64
NGC0525	21.220442	9.703240	0	0	0	2139	30.7	-21.86	0.38	-2.0	1.06
NGC0661	26.060976	28.705988	0	1	0	3815	30.6	-23.19	0.30	-4.4	1.12
NGC0680	27.447035	21.970827	0	1	0	2928	37.5	-24.17	0.34	-4.0	1.16
NGC0770	29.806850	18.954695	0	0	0	2543	36.7	-22.57	0.31	-4.2	0.94
NGC0821	32.088123	10.994870	1	4	0	1718	23.4	-23.99	0.48	-4.8	1.60
NGC0936	36.906090	-1.156280	1	4	0	1429	22.4	-24.85	0.15	-1.2	1.72
NGC1023	40.100052	39.063251	1	8	0	602	11.1	-24.01	0.26	-2.7	1.68
NGC1121	42.663387	-1.734040	0	0	0	2558	35.3	-22.70	0.29	-1.8	0.87
NGC1222	47.236446	-2.955212	0	0	0	2422	33.3	-22.71	0.26	-3.0	1.10
NGC1248	48.202328	-5.224674	0	0	0	2217	30.4	-22.90	0.27	-2.0	1.20
NGC1266	49.003120	-2.427370	0	0	0	2170	29.9	-22.93	0.43	-2.1	1.31
NGC1289	49.707592	-1.973354	0	0	0	2792	38.4	-23.46	0.37	-2.1	1.26
NGC1665	72.071098	-5.427655	0	0	0	2745	37.5	-23.63	0.26	-1.8	1.50
NGC2481	119.307182	23.767693	0	0	0	2157	32.0	-23.38	0.28	0.4	1.02
NGC2549	124.743111	57.803108	1	1	0	1051	12.3	-22.43	0.28	-2.0	1.28
NGC2577	125.681137	22.553040	0	0	0	2062	30.8	-23.41	0.23	-3.0	1.15
NGC2592	126.783669	25.970339	1	1	0	1979	25.0	-22.88	0.25	-4.8	1.09
NGC2594	126.821609	25.878935	0	0	0	2362	35.1	-22.36	0.24	0.0	0.82
NGC2679	132.887192	30.865419	0	0	0	2027	31.1	-22.81	0.14	-2.0	1.35
NGC2685	133.894791	58.734409	0	0	0	875	16.7	-22.78	0.27	-1.0	1.41
NGC2695	133.612778	-3.067101	1	3	0	1833	31.5	-23.64	0.08	-2.1	1.21
NGC2698	133.902222	-3.183882	0	0	0	1900	27.1	-23.32	0.08	-1.0	1.10
NGC2699	133.953415	-3.127507	1	3	0	1868	26.2	-22.72	0.08	-5.0	1.06
NGC2764	137.072983	21.443447	0	0	0	2706	39.6	-23.19	0.17	-2.0	1.09
NGC2768	137.906265	60.037209	1	5	0	1353	21.8	-24.71	0.20	-4.4	1.80
NGC2778	138.101639	35.027424	1	1	0	2025	22.3	-22.23	0.09	-4.8	1.20
NGC2824	139.759277	26.269999	0	0	0	2758	40.7	-22.93	0.14	-2.0	0.86
NGC2852	140.810684	40.163879	0	0	0	1781	28.5	-22.18	0.06	1.0	0.85
NGC2859	141.077286	34.513378	0	0	0	1690	27.0	-24.13	0.09	-1.2	1.43
NGC2880	142.394241	62.490620	1	1	0	1554	21.3	-22.98	0.14	-2.7	1.32
NGC2950	145.646317	58.851219	1	1	0	1322	14.5	-22.93	0.07	-2.0	1.19
NGC2962	145.224609	5.165820	0	3	0	1967	34.0	-24.01	0.25	-1.1	1.39
NGC2974	145.638611	-3.699116	1	3	0	1887	20.9	-23.62	0.23	-4.2	1.58
NGC3032	148.034119	29.236279	1	2	0	1562	21.4	-22.01	0.07	-1.9	1.12
NGC3073	150.216843	55.618935	1	1	0	1173	32.8	-21.78	0.05	-2.8	1.13
NGC3098	150.569458	24.711092	0	0	0	1397	23.0	-22.72	0.16	-1.5	1.12
NGC3156	153.171692	3.129320	1	3	0	1338	21.8	-22.15	0.15	-2.5	1.24

Table 5 (cont'd)

Galaxy	RA (deg)	DEC (deg)	SBF	NED-D	Virgo	$V_{\rm hel}$ (km s^{-1})	D (Mpc)	M_K (mag)	A_B (mag)	T-type	$\log R_{\rm e}$ ($''$)
(1)	(2)	(3)	(4)	(5)	(6)	(7)	(8)	(9)	(10)	(11)	(12)
NGC3182	154.887558	58.205818	0	0	0	2118	34.0	-23.19	0.05	0.4	1.32
NGC3193	154.603683	21.893978	1	3	0	1381	33.1	-24.63	0.11	-4.8	1.42
NGC3226	155.862549	19.898439	1	3	0	1315	22.9	-23.24	0.10	-4.8	1.49
NGC3230	155.933090	12.567883	0	0	0	2795	40.8	-24.18	0.16	-1.8	1.26
NGC3245	156.826523	28.507435	1	1	0	1326	20.3	-23.69	0.11	-2.1	1.40
NGC3248	156.939270	22.847170	0	0	0	1481	24.6	-22.43	0.09	-2.0	1.20
NGC3301	159.233459	21.882166	0	0	0	1339	22.8	-23.28	0.10	-0.4	1.30
NGC3377	161.926666	13.985640	1	10	0	690	10.9	-22.76	0.15	-4.8	1.55
NGC3379	161.956665	12.581630	1	15	0	918	10.3	-23.80	0.11	-4.8	1.60
NGC3384	162.070404	12.629300	1	10	0	733	11.3	-23.52	0.12	-2.7	1.51
NGC3400	162.689590	28.468929	0	0	0	1441	24.7	-21.82	0.08	0.7	1.23
NGC3412	162.722137	13.412142	1	5	0	860	11.0	-22.55	0.12	-2.0	1.49
NGC3414	162.817673	27.974968	1	1	0	1470	24.5	-23.98	0.11	-2.0	1.38
NGC3457	163.702591	17.621157	1	1	0	1148	20.1	-21.89	0.13	-5.0	1.13
NGC3458	164.006042	57.116970	0	0	0	1877	30.9	-23.12	0.04	-2.0	1.06
NGC3489	165.077454	13.901258	1	5	0	695	11.7	-22.99	0.07	-1.2	1.35
NGC3499	165.796280	56.221664	0	0	0	1535	26.4	-21.88	0.04	0.0	0.94
NGC3522	166.668549	20.085621	0	1	0	1228	25.5	-21.67	0.10	-4.9	1.01
NGC3530	167.168411	57.230160	0	0	0	1894	31.2	-22.00	0.04	0.0	0.87
NGC3595	168.856461	47.447147	0	0	0	2177	34.7	-23.28	0.09	-3.3	1.15
NGC3599	168.862305	18.110369	1	3	0	839	19.8	-22.22	0.09	-2.0	1.37
NGC3605	169.194260	18.017141	1	3	0	661	20.1	-21.83	0.09	-4.5	1.23
NGC3607	169.227737	18.051809	1	4	0	942	22.2	-24.74	0.09	-3.1	1.59
NGC3608	169.245697	18.148531	1	4	0	1226	22.3	-23.65	0.09	-4.8	1.47
NGC3610	169.605316	58.786247	1	4	0	1707	20.8	-23.69	0.04	-4.2	1.20
NGC3613	169.650543	57.999924	1	3	0	2051	28.3	-24.26	0.05	-4.7	1.42
NGC3619	169.840088	57.757683	0	0	0	1560	26.8	-23.57	0.08	-0.9	1.42
NGC3626	170.015808	18.356791	1	1	0	1486	19.5	-23.30	0.08	-1.0	1.41
NGC3630	170.070786	2.964170	0	0	0	1499	25.0	-23.16	0.18	-1.5	1.10
NGC3640	170.278549	3.234764	1	4	0	1298	26.3	-24.60	0.19	-4.9	1.49
NGC3641	170.286621	3.194489	1	1	0	1780	25.9	-21.85	0.18	-4.9	0.97
NGC3648	170.631195	39.876972	0	0	0	1970	31.9	-23.06	0.09	-2.0	1.12
NGC3658	170.992706	38.562424	0	0	0	2039	32.7	-23.45	0.09	-2.2	1.28
NGC3665	171.181793	38.762791	0	0	0	2069	33.1	-24.92	0.08	-2.1	1.49
NGC3674	171.610870	57.048290	0	0	0	2055	33.4	-23.23	0.06	-1.9	1.05
NGC3694	172.225571	35.413857	0	0	0	2243	35.2	-22.35	0.10	-5.0	1.02
NGC3757	174.261765	58.415649	0	0	0	1245	22.6	-22.15	0.06	-2.0	0.95
NGC3796	175.129776	60.298958	0	0	0	1250	22.7	-21.84	0.06	0.0	1.06
NGC3838	176.057205	57.948101	0	0	0	1308	23.5	-22.52	0.05	0.0	1.04
NGC3941	178.230667	36.986378	1	2	0	930	11.9	-23.06	0.09	-2.0	1.40
NGC3945	178.307190	60.675560	0	0	0	1281	23.2	-24.31	0.12	-1.2	1.45
NGC3998	179.484039	55.453564	1	2	0	1048	13.7	-23.33	0.07	-2.1	1.30
NGC4026	179.854950	50.961689	1	2	0	985	13.2	-23.03	0.09	-1.8	1.31
NGC4036	180.362045	61.895699	0	0	0	1385	24.6	-24.40	0.10	-2.6	1.46
NGC4078	181.198456	10.595537	0	0	0	2546	38.1	-22.99	0.11	-2.0	0.92
NGC4111	181.763031	43.065392	1	1	0	792	14.6	-23.27	0.06	-1.4	1.08
NGC4119	182.040176	10.378720	0	0	1	1656	16.5	-22.60	0.12	-1.3	1.60
NGC4143	182.400360	42.534218	1	2	0	946	15.5	-23.10	0.05	-1.9	1.39
NGC4150	182.640228	30.401487	1	4	0	208	13.4	-21.65	0.08	-2.1	1.20
NGC4168	183.071808	13.205354	0	1	0	2286	30.9	-24.03	0.16	-4.8	1.48

Table 5 (cont'd)

Galaxy	RA (deg)	DEC (deg)	SBF	NED-D	Virgo	$V_{\rm hel}$ (km s^{-1})	D (Mpc)	M_K (mag)	A_B (mag)	T-type	$\log R_{\rm e}$ ($''$)
(1)	(2)	(3)	(4)	(5)	(6)	(7)	(8)	(9)	(10)	(11)	(12)
NGC4179	183.217087	1.299673	0	0	1	1300	16.5	-23.18	0.14	-1.9	1.30
NGC4191	183.459915	7.200842	0	0	0	2646	39.2	-23.10	0.09	-1.8	1.06
NGC4203	183.770935	33.197243	1	2	0	1087	14.7	-23.44	0.05	-2.7	1.47
NGC4215	183.977142	6.401132	0	0	0	2011	31.5	-23.43	0.07	-0.9	1.18
NGC4233	184.282043	7.624434	0	1	0	2306	33.9	-23.88	0.10	-2.0	1.19
NGC4249	184.497650	5.598720	0	0	0	2618	38.7	-21.98	0.09	-1.3	1.10
NGC4251	184.534607	28.175299	1	1	0	1066	19.1	-23.68	0.10	-1.9	1.29
NGC4255	184.734100	4.785923	0	0	0	1995	31.2	-22.99	0.09	-1.9	1.10
NGC4259	184.842468	5.376242	0	0	0	2497	37.2	-22.19	0.08	-2.0	0.89
NGC4261	184.846924	5.824710	1	5	0	2212	30.8	-25.18	0.08	-4.8	1.58
NGC4262	184.877426	14.877717	2	1	1	1375	15.4	-22.60	0.16	-2.7	1.10
NGC4264	184.899078	5.846804	0	0	0	2518	37.5	-23.00	0.08	-1.1	1.14
NGC4267	184.938675	12.798356	2	1	1	1021	15.8	-23.18	0.20	-2.7	1.58
NGC4268	184.946762	5.283650	0	0	0	2034	31.7	-23.05	0.08	-0.3	1.20
NGC4270	184.955978	5.463371	0	0	0	2331	35.2	-23.69	0.08	-2.0	1.21
NGC4278	185.028320	29.280619	1	9	0	620	15.6	-23.80	0.13	-4.8	1.50
NGC4281	185.089691	5.386430	0	1	0	2671	24.4	-24.01	0.09	-1.5	1.34
NGC4283	185.086609	29.310898	1	3	0	1056	15.3	-21.80	0.11	-4.8	1.09
NGC4324	185.775726	5.250488	0	0	1	1665	16.5	-22.61	0.10	-0.9	1.30
NGC4339	185.895599	6.081713	1	3	1	1266	16.0	-22.49	0.11	-4.7	1.48
NGC4340	185.897141	16.722195	0	2	1	933	18.4	-23.01	0.11	-1.2	1.57
NGC4342	185.912598	7.053936	0	0	1	761	16.5	-22.07	0.09	-3.4	0.82
NGC4346	185.866425	46.993881	1	1	0	832	13.9	-22.55	0.05	-2.0	1.29
NGC4350	185.990891	16.693356	0	2	1	1210	15.4	-23.13	0.12	-1.8	1.23
NGC4365	186.117615	7.317520	2	13	0	1243	23.3	-25.21	0.09	-4.8	1.72
NGC4371	186.230957	11.704288	2	1	1	933	17.0	-23.45	0.16	-1.3	1.47
NGC4374	186.265747	12.886960	2	13	1	1017	18.5	-25.12	0.18	-4.3	1.72
NGC4377	186.301285	14.762218	2	1	1	1338	17.8	-22.43	0.17	-2.6	1.13
NGC4379	186.311386	15.607498	2	2	1	1074	15.8	-22.24	0.10	-2.8	1.27
NGC4382	186.350220	18.191080	2	7	1	746	17.9	-25.13	0.13	-1.3	1.82
NGC4387	186.423813	12.810359	2	3	1	565	17.9	-22.13	0.14	-4.9	1.20
NGC4406	186.549225	12.945970	2	15	1	-224	16.8	-25.04	0.13	-4.8	1.97
NGC4417	186.710938	9.584117	2	1	1	828	16.0	-22.86	0.11	-1.9	1.25
NGC4425	186.805664	12.734803	0	0	1	1908	16.5	-22.09	0.13	-0.6	1.38
NGC4429	186.860657	11.107540	0	0	1	1104	16.5	-24.32	0.14	-1.1	1.62
NGC4434	186.902832	8.154311	2	5	0	1070	22.4	-22.55	0.10	-4.8	1.16
NGC4435	186.918762	13.079021	2	0	1	791	16.7	-23.83	0.13	-2.1	1.49
NGC4442	187.016220	9.803620	2	1	1	547	15.3	-23.63	0.09	-1.9	1.44
NGC4452	187.180417	11.755000	0	2	1	188	15.6	-21.88	0.13	-2.0	1.30
NGC4458	187.239716	13.241916	2	8	1	677	16.4	-21.76	0.10	-4.8	1.37
NGC4459	187.250107	13.978580	2	3	1	1192	16.1	-23.89	0.19	-1.4	1.56
NGC4461	187.262543	13.183857	0	0	1	1924	16.5	-23.08	0.10	-0.8	1.40
NGC4472	187.444992	8.000410	2	18	1	981	17.1	-25.78	0.10	-4.8	1.98
NGC4473	187.453659	13.429320	2	8	1	2260	15.3	-23.77	0.12	-4.7	1.43
NGC4474	187.473099	14.068673	2	1	1	1611	15.6	-22.28	0.18	-2.0	1.30
NGC4476	187.496170	12.348669	2	3	1	1968	17.6	-21.78	0.12	-3.0	1.20
NGC4477	187.509048	13.636443	0	0	1	1338	16.5	-23.75	0.14	-1.9	1.59
NGC4478	187.572662	12.328578	2	9	1	1375	17.0	-22.80	0.10	-4.8	1.20
NGC4483	187.669250	9.015665	2	1	1	906	16.7	-21.84	0.09	-1.3	1.24
NGC4486	187.705933	12.391100	2	15	1	1284	17.2	-25.38	0.10	-4.3	1.91

Table 5 (cont'd)

Galaxy	RA (deg)	DEC (deg)	SBF	NED-D	Virgo	$V_{\rm hel}$ (km s^{-1})	D (Mpc)	M_K (mag)	A_B (mag)	T-type	$\log R_{\rm e}$ ($''$)
(1)	(2)	(3)	(4)	(5)	(6)	(7)	(8)	(9)	(10)	(11)	(12)
NGC4486A	187.740540	12.270361	2	0	1	758	18.3	-21.82	0.10	-5.0	0.94
NGC4489	187.717667	16.758696	2	5	1	961	15.4	-21.59	0.12	-4.8	1.42
NGC4494	187.850143	25.774981	1	9	0	1342	16.6	-24.11	0.09	-4.8	1.69
NGC4503	188.025803	11.176434	0	0	1	1334	16.5	-23.22	0.22	-1.8	1.45
NGC4521	188.198853	63.939293	0	0	0	2511	39.7	-23.92	0.08	-0.1	1.21
NGC4526	188.512619	7.699140	1	5	1	617	16.4	-24.62	0.10	-1.9	1.65
NGC4528	188.525269	11.321266	2	0	1	1378	15.8	-22.05	0.20	-2.0	1.15
NGC4546	188.872940	-3.793227	1	2	0	1057	13.7	-23.30	0.15	-2.7	1.40
NGC4550	188.877548	12.220955	2	3	1	459	15.5	-22.27	0.17	-2.1	1.19
NGC4551	188.908249	12.264010	2	5	1	1176	16.1	-22.18	0.17	-4.9	1.22
NGC4552	188.916183	12.556040	2	12	1	344	15.8	-24.29	0.18	-4.6	1.53
NGC4564	189.112473	11.439320	2	5	1	1155	15.8	-23.08	0.14	-4.8	1.31
NGC4570	189.222504	7.246663	2	1	1	1787	17.1	-23.48	0.09	-2.0	1.30
NGC4578	189.377274	9.555121	2	3	1	2292	16.3	-22.66	0.09	-2.0	1.51
NGC4596	189.983063	10.176031	0	0	1	1892	16.5	-23.63	0.09	-0.9	1.59
NGC4608	190.305374	10.155793	0	0	1	1850	16.5	-22.94	0.07	-1.9	1.42
NGC4612	190.386490	7.314782	2	1	1	1775	16.6	-22.55	0.11	-2.0	1.40
NGC4621	190.509674	11.646930	2	9	1	467	14.9	-24.14	0.14	-4.8	1.63
NGC4623	190.544601	7.676934	2	1	1	1807	17.4	-21.74	0.10	-1.5	1.31
NGC4624	191.274826	3.055684	0	0	1	912	16.5	-23.67	0.10	-0.6	1.64
NGC4636	190.707779	2.687780	1	11	0	930	14.3	-24.36	0.12	-4.8	1.95
NGC4638	190.697632	11.442459	2	2	1	1152	17.5	-23.01	0.11	-2.7	1.22
NGC4643	190.833893	1.978399	0	0	1	1333	16.5	-23.69	0.13	-0.6	1.38
NGC4649	190.916702	11.552610	2	11	1	1110	17.3	-25.46	0.11	-4.6	1.82
NGC4660	191.133209	11.190533	2	5	1	1087	15.0	-22.69	0.15	-4.7	1.09
NGC4684	191.822861	-2.727538	1	1	0	1560	13.1	-22.21	0.12	-1.2	1.32
NGC4690	191.981323	-1.655975	0	0	0	2765	40.2	-22.96	0.13	-3.0	1.25
NGC4694	192.062881	10.983624	0	0	1	1171	16.5	-22.15	0.17	-2.0	1.47
NGC4697	192.149612	-5.800850	1	8	0	1252	11.4	-23.93	0.13	-4.4	1.79
NGC4710	192.412323	15.165490	0	0	1	1102	16.5	-23.53	0.13	-0.9	1.48
NGC4733	192.778259	10.912103	1	1	1	925	14.5	-21.80	0.09	-3.8	1.52
NGC4753	193.092133	-1.199690	1	3	0	1163	22.9	-25.09	0.14	-1.4	1.69
NGC4754	193.073181	11.313660	2	3	1	1351	16.1	-23.64	0.14	-2.5	1.50
NGC4762	193.233536	11.230800	0	2	0	986	22.6	-24.48	0.09	-1.8	1.64
NGC4803	193.890289	8.240547	0	0	0	2645	39.4	-22.28	0.13	0.0	0.94
NGC5103	200.125229	43.084015	0	0	0	1273	23.4	-22.36	0.08	0.0	1.02
NGC5173	202.105301	46.591572	0	0	0	2424	38.4	-22.88	0.12	-4.9	1.01
NGC5198	202.547546	46.670830	0	0	0	2519	39.6	-24.10	0.10	-4.8	1.38
NGC5273	205.534943	35.654240	1	2	0	1085	16.1	-22.37	0.04	-1.9	1.57
NGC5308	206.751633	60.973038	0	6	0	1998	31.5	-24.13	0.08	-2.1	1.25
NGC5322	207.313339	60.190411	1	5	0	1780	30.3	-25.26	0.06	-4.8	1.60
NGC5342	207.857910	59.863014	0	0	0	2189	35.5	-22.61	0.05	-2.0	0.97
NGC5353	208.361420	40.283123	0	0	0	2198	35.2	-25.11	0.05	-2.1	1.30
NGC5355	208.439850	40.338795	0	0	0	2344	37.1	-22.40	0.05	-2.1	1.06
NGC5358	208.501801	40.277420	0	0	0	2412	38.0	-22.01	0.04	-0.2	1.05
NGC5379	208.893112	59.742825	0	0	0	1774	30.0	-22.08	0.08	-2.0	1.32
NGC5422	210.175262	55.164478	0	0	0	1838	30.8	-23.69	0.06	-1.5	1.33
NGC5473	211.180176	54.892620	0	0	0	2022	33.2	-24.25	0.05	-2.7	1.32
NGC5475	211.301437	55.741802	0	0	0	1671	28.6	-22.88	0.05	1.0	1.22
NGC5481	211.671722	50.723320	0	2	0	1989	25.8	-22.68	0.08	-3.9	1.35

Table 5 (cont'd)

Galaxy	RA (deg)	DEC (deg)	SBF	NED-D	Virgo	$V_{\rm hel}$ (km s^{-1})	D (Mpc)	M_K (mag)	A_B (mag)	T-type	$\log R_{\rm e}$ ($''$)
(1)	(2)	(3)	(4)	(5)	(6)	(7)	(8)	(9)	(10)	(11)	(12)
NGC5485	211.797134	55.001518	1	3	0	1927	25.2	-23.61	0.07	-2.0	1.45
NGC5493	212.872421	-5.043663	0	0	0	2665	38.8	-24.49	0.15	-2.1	1.14
NGC5500	212.563522	48.546066	0	0	0	1914	31.7	-21.93	0.09	-4.9	1.18
NGC5507	213.332825	-3.148860	0	0	0	1851	28.5	-23.19	0.26	-2.3	1.09
NGC5557	214.607117	36.493690	0	3	0	3219	38.8	-24.87	0.03	-4.8	1.46
NGC5574	215.233109	3.237995	1	1	0	1589	23.2	-22.30	0.13	-2.8	1.13
NGC5576	215.265381	3.271049	1	3	0	1506	24.8	-24.15	0.13	-4.8	1.34
NGC5582	215.179703	39.693584	1	3	0	1430	27.7	-23.28	0.06	-4.9	1.44
NGC5611	216.019897	33.047501	1	1	0	1968	24.5	-22.20	0.05	-1.9	1.00
NGC5631	216.638687	56.582664	1	1	0	1944	27.0	-23.70	0.09	-1.9	1.32
NGC5638	217.418289	3.233443	1	3	0	1652	25.6	-23.80	0.14	-4.8	1.45
NGC5687	218.718201	54.475685	1	1	0	2143	27.2	-23.22	0.05	-3.0	1.36
NGC5770	223.312653	3.959721	1	1	0	1471	18.5	-22.15	0.17	-2.0	1.23
NGC5813	225.296936	1.701970	1	4	0	1956	31.3	-25.09	0.25	-4.8	1.76
NGC5831	226.029266	1.219917	1	3	0	1645	26.4	-23.69	0.25	-4.8	1.40
NGC5838	226.359467	2.099356	0	0	0	1341	21.8	-24.13	0.23	-2.6	1.40
NGC5839	226.364471	1.634633	1	1	0	1220	22.0	-22.53	0.23	-2.0	1.22
NGC5845	226.503281	1.633824	1	2	0	1472	25.2	-22.92	0.23	-4.9	0.80
NGC5846	226.621887	1.605637	1	6	0	1712	24.2	-25.01	0.24	-4.7	1.77
NGC5854	226.948853	2.568560	0	0	0	1663	26.2	-23.30	0.23	-1.1	1.26
NGC5864	227.389786	3.052741	0	0	0	1874	29.0	-23.62	0.19	-1.7	1.35
NGC5866	226.623169	55.763309	1	3	0	755	14.9	-24.00	0.06	-1.3	1.56
NGC5869	227.456055	0.469967	0	1	0	2065	24.9	-23.27	0.24	-2.3	1.31
NGC6010	238.579773	0.543033	0	0	0	2022	30.6	-23.53	0.45	0.4	1.16
NGC6014	238.989105	5.931838	0	0	0	2381	35.8	-22.99	0.22	-1.9	1.35
NGC6017	239.314529	5.998364	1	1	0	1788	29.0	-22.52	0.23	-5.0	0.85
NGC6149	246.851151	19.597290	0	0	0	2427	37.2	-22.60	0.30	-1.9	1.03
NGC6278	255.209763	23.010956	0	0	0	2832	42.9	-24.19	0.27	-1.9	1.22
NGC6547	271.291748	25.232645	0	0	0	2677	40.8	-23.60	0.50	-1.3	1.06
NGC6548	271.496826	18.587217	1	1	0	2208	22.4	-23.19	0.35	-1.9	1.35
NGC6703	281.828522	45.550648	1	4	0	2373	25.9	-23.85	0.37	-2.8	1.34
NGC6798	291.013306	53.624752	0	0	0	2360	37.5	-23.52	0.57	-2.0	1.23
NGC7280	336.614899	16.148266	1	2	0	1845	23.7	-22.83	0.24	-1.3	1.33
NGC7332	339.352173	23.798351	1	1	0	1197	22.4	-23.75	0.16	-1.9	1.24
NGC7454	345.277130	16.388371	1	3	0	2020	23.2	-23.00	0.33	-4.7	1.41
NGC7457	345.249725	30.144892	1	3	0	844	12.9	-22.38	0.23	-2.6	1.56
NGC7465	345.503967	15.964876	0	0	0	1960	29.3	-22.82	0.33	-1.9	0.90
NGC7693	353.293671	-1.292010	0	0	0	2502	35.4	-21.58	0.15	-1.0	1.11
NGC7710	353.942261	-2.880941	0	0	0	2407	34.0	-21.99	0.15	-1.9	0.92
PGC016060	72.143387	-3.867104	0	0	0	2764	37.8	-22.64	0.19	-0.6	1.01
PGC028887	149.931290	11.660812	0	0	0	2833	41.0	-22.26	0.17	0.0	1.08
PGC029321	151.463226	12.961213	0	0	0	2816	40.9	-21.66	0.16	0.0	0.89
PGC035754	173.614716	33.178913	0	0	0	2534	39.0	-21.90	0.11	-3.0	0.83
PGC042549	190.316513	-5.009177	0	0	0	2822	40.7	-22.71	0.11	-5.0	1.06
PGC044433	194.578110	13.391409	0	0	0	2675	40.1	-22.25	0.13	0.0	0.71
PGC050395	211.913544	54.794575	0	0	0	2322	37.2	-21.92	0.05	0.0	1.04
PGC051753	217.310318	44.699104	0	0	0	2418	38.3	-21.92	0.05	0.0	1.01
PGC054452	228.894180	2.248187	0	0	0	1918	29.5	-21.59	0.18	-2.0	1.14
PGC056772	240.548340	7.085953	0	0	0	2655	39.5	-22.06	0.19	-2.0	0.93
PGC058114	246.517838	2.906550	0	0	0	1507	23.8	-21.57	0.29	-2.0	0.97

Table 5 (cont'd)

Galaxy	RA (deg)	DEC (deg)	SBF	NED-D	Virgo	$V_{\rm hel}$ (km s^{-1})	D (Mpc)	M_K (mag)	A_B (mag)	T-type	$\log R_{\rm e}$ ($''$)
(1)	(2)	(3)	(4)	(5)	(6)	(7)	(8)	(9)	(10)	(11)	(12)
PGC061468	272.360748	19.117682	0	0	0	2371	36.2	-21.68	0.35	0.0	1.06
PGC071531	352.121338	19.863962	0	0	0	2030	30.4	-21.74	0.53	-4.0	0.88
PGC170172	176.731720	-5.187745	0	0	0	2562	37.1	-21.89	0.08	-5.0	0.89
UGC03960	115.094856	23.275089	0	0	0	2255	33.2	-21.89	0.20	-4.9	1.24
UGC04551	131.024582	49.793968	0	0	0	1728	28.0	-22.92	0.10	-2.0	1.03
UGC05408	150.966095	59.436138	0	0	0	2998	45.8	-22.03	0.06	-3.3	0.84
UGC06062	164.656662	9.050468	0	0	0	2634	38.7	-22.82	0.13	-2.0	1.05
UGC06176	166.852753	21.657185	0	0	0	2677	40.1	-22.66	0.08	-2.0	1.03
UGC08876	209.241943	45.973179	0	0	0	2085	33.9	-22.37	0.04	-0.1	0.93
UGC09519	221.588028	34.370651	0	0	0	1631	27.6	-21.98	0.09	-1.9	0.87

Note. — Column (1): The Name is the principal designation from LEDA, which is used as standard designation for our project. Column (2): Right Ascension in degrees and decimal (J2000.0). Column (3): Declination in degrees and decimals (J2000.0). As the galaxy names may not be always consistent between different catalogues, these coordinate *define* the galaxies of the sample. Column (4): $\rm SBF = 1$ if the galaxy is in Tonry et al. (2001) and $\rm SBF = 2$ if it is in Mei et al. (2007) or both. Column (5): number of redshift-independent distance determinations listed in the NED-D catalogue, excluding the ones based on kinematical scaling relations. Column (6): $\rm Virgo = 1$ if the galaxies is contained within a sphere of radius $R = 3.5$ Mpc from the center of the cluster assumed at coordinates RA=12h28m19s and DEC=+12°40′ (Mould et al. 2000) and distance $D = 16.5$ Mpc (Mei et al. 2007). Column (7): Heliocentric velocity measured from the SAURON integral-field stellar kinematics (1σ error $\Delta V_{\rm hel} = 5$ km s^{-1}). Column (8): distance in Mpc. When $\rm SBF = 1$ the distance comes from Tonry et al. (2001), corrected by *subtracting* 0.06 mag to the distance modulus (Mei et al. 2007); When $\rm SBF = 2$ the distance comes from Mei et al. (2007); When $\rm SBF = 0$ and NED-D > 0 the distance is the median of the NED-D values, excluding the ones based on kinematical scaling relations; When $\rm SBF = NED\text{-}D = 0$ and the galaxy is in Virgo ($\rm Virgo = 1$) then it is assigned the cluster distance $D = 16.5$ Mpc (Mei et al. 2007); Otherwise $D = V_{\rm cosmic}/H_0$, with $H_0 = 72$ km s^{-1} Mpc^{-1}, where $V_{\rm cosmic}$ is the velocity derived from $V_{\rm hel}$ via the local flow field model of Mould et al. (2000) using only the Virgo attractor. Column (9): total galaxy absolute magnitude derived from the apparent magnitude K_T (2MASS keyword k_m_ext) at the adopted distance D and corrected for the foreground galactic extinction: $M_K = K_T - 5\log_{10} D - 25 - A_B/11.8$, which assumes $A_B/A_K = 11.8$. Column (10): B-band foreground galactic extinction from Schlegel et al. (1998). Column (11): Morphological T-type from HyperLeda. E: $T \leq -3.5$, S0: $-3.5 < T \leq -0.5$. This morphology was *not* the one used for the sample selection, but is printed in Fig. 5 and 6. Column (12): Projected half-light effective radius. It was derived from a combination of RC3 and 2MASS determinations, which both use growth curves, as described in Section 4.1, but it was normalized to agree on average with RC3.

Table 6. The 611 spiral galaxies in the ATLAS^{3D} *parent* sample.

Galaxy	RA (deg)	DEC (deg)	SBF	NED-D	Virgo	$V_{\rm hel}$ (km s^{-1})	D (Mpc)	M_K (mag)	A_B (mag)	T-type	$\log R_{\rm e}$ ($''$)
(1)	(2)	(3)	(4)	(5)	(6)	(7)	(8)	(9)	(10)	(11)	(12)
IC0065	15.230966	47.681984	0	0	0	2614	39.7	-23.54	0.64	4.0	1.38
IC0163	27.312431	20.711317	0	0	0	2749	39.7	-22.38	0.36	8.0	1.35
IC0239	39.116250	38.970000	0	0	0	903	15.7	-22.23	0.31	6.0	1.90
IC0540	142.542755	7.902529	0	0	0	2035	30.0	-21.89	0.26	3.5	1.08
IC0591	151.865479	12.274520	0	0	0	2839	41.2	-21.82	0.15	6.0	1.19
IC0610	156.618179	20.228252	0	0	0	1170	19.6	-21.53	0.09	3.9	1.02
IC0750	179.717606	42.722404	0	1	0	701	36.8	-24.71	0.09	2.1	1.24
IC0777	184.849228	28.309881	0	0	0	2541	39.0	-21.92	0.10	2.6	0.95
IC0800	188.486313	15.354542	0	0	0	2326	35.8	-22.20	0.16	5.2	1.56
IC0851	197.143127	21.049742	0	0	0	2615	39.8	-21.82	0.15	3.1	1.31

Note. — The meaning of the columns is the same as in Table 5, except for Column (7), which contain here the heliocentric velocity taken from NED. Only the first 10 rows are shown while the full 611 will be published electronically. Both Table 5 and 6 are also available from our project website http://purl.com/atlas3d.